Journal of Materials Chemistry C

Accepted Manuscript

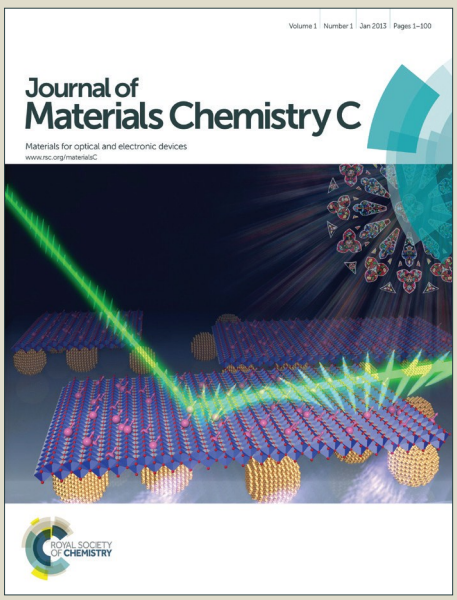

ROYAL SOCIETY OF CHEMISTRY

www.rsc.org/materialsC

Bifunctional Superparamagnetic-Luminescent Core/Shell/Satellite Structured Microspheres: Preparation, Characterization, and Magnetodisplay Application

Chung-Lin Li[1], Bohr-Ran Huang[2], Jia-Yaw Chang[3], Jem-Kun Chen[1]*

1Department of Materials Science and Engineering, National Taiwan University of Science and Technology, 43, Sec. 4, Keelung Road, Taipei, 106, Taiwan, Republic of China

[2]Department of Electrical Engineering, National Taiwan University of Science and Technology, 43, Sec 4, Keelung Rd, Taipei, 106, Taiwan, Republic of China

[3]Department of Chemical Engineering, National Taiwan University of Science and Technology, 43, Sec 4, Keelung Rd, Taipei, 106, Taiwan, Republic of China

*To whom correspondence should be addressed.

Tel.: +886-2-27376523

Fax: +886-2-27376544

E-mail: jkchen@mail.ntust.edu.tw

Abstract

We present a general process that allows convenient production of bifunctional superparamagnetic-luminescent composite particles (CPs) by direct self-assembly of nanoparticles on host 3-μm silicon oxide microspheres (SiMS). Fe_3O_4 nanoparticles (FeNPs) can be directly assembled lay-by-lay (LBL) with a dithiol agent onto the host surface that modified high-density surface thiol groups through the strong coordination interactions between metal cations and thiol groups. The resulting structures can be further conveniently overcoated with a layer of normal silica with thiol groups to stabilize the assemblies and immobilize CdTe quantum dots (QDs). As the entire fabrication process does not involve complicated surface modification procedures, the rich thiol groups among FeNPs and CdTe QDs are not disturbed significantly. Therefore, core/shell/satellite structured SiMS/FeNPs/CdTe CPs retain their original properties including highly efficient superparamagnetic and luminescence. A home-made transparent sandwich device with solenoid coils (TSDSC) contained the aqueous dispersions of these CPs to observe reversible magnetically responsive transmittance and luminescence due to the particle chaining behavior in presence of an altering magnetic field (AMF). The results suggest that specific superparamagnetic and luminescence of nanoparticles can efficiently endued on microscale particles. Such assembly approach will provide the research community a highly versatile, configurable, scalable, and reproducible process for the preparation of various multifunctional structures.

Keywords: core/shell/satellite; CdTe quantum dots; iron oxide nanoparticle; silica spherical particles; particle chaining behavior

Introduction

In recent years, core/shell-structured composite materials,[1] which combine with the advantageous properties of both materials of the core and the shell, have attracted increasing interest to materials scientists due to their unique physicochemical properties and great potential applications in the areas of rheology,[2] photonics,[3] catalysis,[4] biotechnology,[5] and nanotechnology[6]. These specific core/shell structures which possess the ability to be modified with different charges, functions, or reactive moieties on the surface with enhanced stability and compatibility provide an avenue for the synthesis of complex composite materials. Alternatively, various types of bifunctional or trifunctional core/shell materials, such as electronic/optical, electronic/catalytic, magnetic/electronic, etc., could be technically obtained.[7] Among these core/shell/satellite-structured composite materials are typical spherical particle, the structures comprise a core material, a shell layer, and the satellite particles for multifunctional particles [8]. These properties can be modified by choosing either the constituting materials or changing the ratio of the core to shell to satellite. The resulting composites often combine large spherical particles with nanoparticles (NPs). Fabricating core/shell nanostructures is based on the combination of solvent-controlled precipitation[9] and layer-by-layer (LBL) adsorption[10,11] of oppositely charged macromolecules on colloidal templates (cores).

SiO_2-coated particles have been attracted much attention, because these core−shell particles have potential applications in catalysis, drug delivery, and colloidal crystals.[12,13] As a coating material, SiO_2 has many versatile properties. First of all, SiO_2 is hydrophilic and negatively charged, which can prevent the aggregation of the colloidal particles. Hollow silica structures could be obtained by removing the core material via calcination or leaching, because the SiO_2 is chemically very stable. Furthermore, SiO_2 has also a tunable controlled porosity, biocompatibility, optical transparency, and mechanical stability to immobilize matal nanoparticles.[14−16] Thus, SiO_2 is considered as an ideal and low-cost material that has already been used for coating on various core particles, such as metal colloids (e.g., Au, Ag),[17] magnetic particles (e.g., Fe_3O_4),[18] semiconductor nanocrystals (e.g., CdTe),[19] and polymers (e.g., polystyrene).[20−22] Among these particles, magnetite (Fe_3O_4) has been widely studied because of their potential applications as ferrofluids,[23−25] biological assays,[26] and chemical sensors.[27] In addition, Semiconductor quantum dots (QDs) could also serve as optical probes and biorecognition process for in vitro imaging with a number of advantages, for example, high emission intensity, photostability, and a single excitation wavelength for multiple colors over conventional dyes.

Multifunctional particles in the micrometer scale that exhibit two or more

different properties are highly desirable for many important technological applications.[28−31] For example, microspheres embedded with magnetic iron oxide nanoparticles and fluorescent quantum dots have been widely studied as a multiple-mode imaging contrast agents combining magnetic resonance with optical detection and biological targeting.[32,33] Although superparamagnetic and luminescent QDs preserve separately their irreplaceable properties, they cannot realize multiple functions. It is necessary to constitute a multifunctional nanoplatform by integrating multiple nanoparticle components into a single system by rational assembly and hybridization techniques. Multi- or bifunctional nanomaterials, in which several different materials are mixed on the nanoscale, can show not only combined properties of the original components but also possess novel and collective performances not seen in the original components.[34] In this work, we explore a LBL assembly technique for the fabrication of bifunctional (superparamagnetic and luminescent) composite nanostructures of microspheres. Briefly, 3-μm SiO_2 microspheres modified by thiol groups are first synthesized as adsorbent hosts, named as SiMS. Fe_3O_4 nanoparticles (FeNPs) are synthesized separately, and then efficiently assembled on the surface of SiMS by taking advantage of the high density thiol groups through LBL (using a dithiol linking agent)[23,35]. In order to improve the chemical stability of assembled FeNPs layers and water-dispersibility, the composites

particles (CPs) were further coated with a thin shell of mercapto-silica. Sequentially, CdTe QDs were deposited on the CPs for preparation of core/shell/satellite SiMS@FeNPs@CdTe CPs. (Scheme 1) The resulting CPs are dispersed in aqueous solution to encapsulate into a home-made transparent sandwich device with solenoid coils (TSDSC) to observe the superparamagnetic and luminescent properties. Chaining of magnetic nanomaterials has been reported in other media (e.g., water or insulating oils), soft condensed matter phases for example.[36, 37] Because of nontoxic, cheap and low viscosity, we dispersed CPs in water to result low response time in presence of magnetic field for commercial application. Upon applying an alternating magnetic field (AMF) to the TSDSCs, these CPs were strung with neighborhood particle in a linear feature along the direction of the AMF applying, resulting in significant change in transmittance and luminescence. These aqueous suspensions might be suitable for application in magnetodisplay applications.

Experimental section

Materials

Silica microspheres (SiMS, ca. 3 μm) were purchased from Polysciences. Tetraethyl orthosilicate (TEOS, 98%), 1,6-dimercaptohexane (cross-linking agent, DMH, 96%) and (3-mercaptopropyl)trimethoxysilane (MPS, 95%) were obtained from Sigma–Aldrich and purified through vacuum distillation prior to use. Iron(II)

chloride tetrahydrate ($FeCl_2 \cdot 4H_2O$, 98%), iron(III) chloride hexahydrate ($FeCl_3 \cdot 6H_2O$, 97%), and aqueous ammonium hydroxide (NH_4OH, 28%) were purchased from Acros Organics. Tellurium powder (Te, 99.99 %), and cadmium chloride hemipentahydrate ($CdCl_2 \cdot 2.5H_2O$, 99%) were obtained from Sigma-Aldrich. Thioglycolic acid (TA, 98%) and 2-mercaptoethanol were obtained from Fisher Scientific. All other chemicals and solvents were reagent grade and used without further purification.

Synthesis of Core/Shell/Satellite SiMS/FeNPs/CdTe CPs

Scheme 1 illustrates the main strategy of synthesis for core/shell/satellite SiMS/FeNPs/CdTe CPs. Firstly, 3-μm SiMS (0.52 mg), dispersed in anhydrous toluene (10 mL) with stirring for 30 min, was heated at 80 °C with a oil bath under N_2 atmosphere. MPS (0.22 mL) was added dropwise into the SiMS solution to modify the SiMS with thiol groups for 60 min [38]. After and removing the supernatant solution, the resulting MPS-modified SiMS were collected with a centrifuge, and washed alternately with toluene and EtOH to remove excess MPS. The resulting MPS-modified SiMS were dried and redispersed in aqueous solution. FeNPs suspension (20 mL), synthesized according to a pervious study[39], was added dropwise slowly to the solution of MPS-modified SiMS (0.13 mg/mL) for 24 h. The samples, denoted as SiMS@FeNP1, were washed with water and EtOH to remove any unreacted components, and collected by a permanent magnet (0.48T). DMH (0.3

mL) in anhydrous toluene (10 mL) was added dropwise slowly to the aqueous solution of SiMS@FeNP1 (10 mL) for 30 min to modify the FeNP1 layer with thiol groups repeatedly on the surface.[40] The FeNPs solution was added dropwise to the DMH-modified SiMS@FeNP1 CPs to assemble second FeNPs layer onto the CPs, denoted as SiMS@FeNP2. The procedure, regarded as LBL technique, was repeated to assemble FeNPs multi-layers on the SiMS. The descriptor SiMs@FeNP(number) is employed herein to describe the species featuring various layers of FeNPs on the SiMS. The SiMS@FeNPs CPs were dispersed in the solution of EtOH and ammonium hydroxide solution (4:1 v/v), and purged with N_2 for 20 min. Mixture of TEOS (0.04 M) and MPS (0.01 M) were added dropwise slowly into the solution of SiMS@FeNPs CPs for 3 h to generate a buffer layer with thiol groups onto the surface. The resulting sample was washed alternately with water and EtOH for three times to remove excess MPS. The MPS-modified SiMS@FeNPs@SiO_2 CPs were redispersed in the water and kept in dark for further use.

In addition, black tellurium powder (1.02 mmol) was dispersed with 3.0 mL water in a flask to mix with $NaBH_4$ (3.2 mmol) aqueous solution in ice bed for 2 h under negative room pressure to remove the product of H_2. The entire mixture turned from black to colorless, indicating the formation of NaHTe. The resulting solution was added to a basic solution (pH 10) including cadmium chloride (2.3 mmol) and TA

(4.63 mmol) at 100°C for 20 h. The resulting samples were reprecipitated in acetone to collect CdTe QDs by centrifugation at 6000 rpm for 30 min. After the purification processes for three cycles, the TA-stabilized CdTe QDs were redispersed in water and kept in dark for further use. Hydrodynamic size of the CdTe QDs was ca. 7.4 nm, obtained by dynamic light scattering measurement (DLS, Malvern Nano-s90). The aqueous solution (10 mL) of TA-stabilized CdTe QDs was added dropwise to the aqueous solution (20 mL) of MPS-modified SiMS@FeNPs@SiO_2 CPs with stirring at pH 11 for 4 h. The resulting samples were washed with water repeatedly after centrifugation to remove unreacted components. The CdTe QDs were immobilized onto the SiMS@FeNPs@SiO_2 surface to form the core/shell/satellite structured CPs, denoted as SiMS@FeNPs@SiO_2@CdTe.

Characterization of SiMS@FeNPs@SiO_2@CdTe CPs

Fourier transform infrared (FTIR) and UV–Vis spectroscopy were performed using a Digilab-FTS1000 instrument and a Jasco V-670 UV-Vis/NIR spectrophotometer. The photoluminescence measurement was performed with the Jasco FP-8500 instrument at 400 nm of excitation wavelength. The rhodamine 6 G (95 % quantum yield) was employed to integrate the luminescence intensities of the QDs and SiMS@FeNPs@SiO_2@CdTe. X-ray diffraction (D2 PHASER X-ray Diffractometer, Bruker) was employed to analyze the crystallite size and structure of

these samples using Cu target radiation (300 W) over a 2θ range from 10 to 80°. The magnetic properties were measured at room temperature using a superconducting quantum interference device magnetometer (SQUID, Quantum Design, MPMS7). Scanning electron microscopy (SEM) and elemental analyses were performed using a field-emission scanning electron microscope (JEOL JSM-6500F) with energy dispersive X-ray spectroscopy (EDX). Transmission electron microscopy (TEM) images were obtained using a field-emission transmission electron microscope (Philips Tecnai G2 F20) operated at an accelerating voltage of 200 kV. The strength of the magnetic field was recorded using a Gauss meter (Lutron MG-3002 AC/DC magnetic meter). The confocal laser scanning microscopy (CLSM, Leica TCS SP5) was employed to observe the 3D distribution of luminescent and magnetic CPs in the absence and presence of AMF. The excitation light (Ar laser, wavelength 514 nm, 10 mW) was exploited to observe luminescence of the samples in aqueous solutions.

Fabrication of TSDSC Encapsulating Aqueous Solutions of SiMS@FeNPs@SiO_2@CdTe CPs

We fabricated and performed of a sandwich structured magnetodisplay consisting a ring-shaped Teflon spacer (thickness: 100 μm; DuPont) between two transparent acrylic plates with Teflon coating (layer thickness: 60 nm; AF1600, DuPont; transparency : 90.6%) (Scheme 2). A solenoid coil (copper wire, resistance:

0.59 v/a; line width: 0.27 mm; coil diameter: 22 mm; number of coils: 60) was wrapped round the megnetodisplay to obtain the TSDSC. The solenoid coil was connected to a power supply (Twintex, TP-1303) and a function generator (Agilent Technologies, 33220A) linking with an amplifier (A.A. Lab Systems, A-303) to generate AMFs. The TSDSC were placed between a W–Kr lamp source (StellarNet, SL1) and an optical spectrometer (StellarNet CXR-25) equipped charge-coupled device (CCD; Toshiba, 3648-element) and integrating sphere (radius: 50 mm) to monitor the transmittance change in the range of wavelength from 350 to 2300 nm. The apparatus for the dynamic image acquisition system comprised an inverted microscope (Nikon Eclipse FN1) and a computer with the image processing software (Image-Pro Plus V7). Light was scattered by the dispersed CPs in the absence of AMF, leading to an opaque of TSDSC (Scheme 2). A transparency of TSDSC appeared with particle chaining in the presence of AMF. Various concentrations of the suspensions were injected into the area defined by the ring-shaped spacer and two acrylic sheets to evaluate the transmittance change between dispersing and chaining state. 5.8 wt % of aqueous solutions of CPs was determined as the optimal concentration to fill the TSDSC due to the apparent luminescence and transmittance change.

Complex Magnetic Permeability of SiMS@FeNPs@SiO_2@CdTe CPs

Physical properties of nanostructures constructed of nanoparticles (NPs), which are those of neither the bulk metal nor the molecular components, strongly depend on the particle size, interparticle distance, nature of the protecting organic shell, and shape of the NPs [41]. The complex magnetic permeability is a useful tool for dealing with changes in physical property for SiMS@FeNPs@SiO_2@CdTe CPs. The permeability was consists of a real part (in phase) and an imaginary part (out of phase) dependent on the frequency. For layered spherical particles, the complex magnetic permittivity (μ_{cs}) in the Clausius-Mossoti factor, can be described as [23, 42]

$$\tilde{\mu}_{\mathrm{cs}} = \tilde{\mu}_{\mathrm{ext}} \left\{ \frac{\left[R^3 + 2\left(\frac{\tilde{\mu}_{\mathrm{int}} - \tilde{\mu}_{\mathrm{ext}}}{\tilde{\mu}_{\mathrm{int}} + 2\tilde{\mu}_{ext}} \right) \right]}{\left[R^3 - \left(\frac{\tilde{\mu}_{\mathrm{int}} - \tilde{\mu}_{\mathrm{ext}}}{\tilde{\mu}_{\mathrm{int}} + 2\tilde{\mu}_{\mathrm{ext}}} \right) \right]} \right\} \quad (1)$$

where R is equal to the ratio of radius as defined r_2/r_1, where r_2 is the radius of the whole particle and r_1 is the radius of the core particle. $\tilde{\mu}_{\mathrm{int}}$ and $\tilde{\mu}_{\mathrm{ext}}$ are the complex magnetic permittivities of the core and shell layer, respectively. In this study, the particles were driven by dipole–dipole interplay in a magnetic field; because they were required only to hide behind the neighboring tip particles, they traveled relatively short distances. By setting suitable parameters for the device thickness, particle size, and concentration of magnetizable composite particles, the response speed could reach values comparing favorably with those of the magnetodisplays.

Results and Discussions

Characterization of SiMS@FeNPs@SiO_2@CdTe CPs

Figure 1 represents the FTIR spectra of SiMS, MPS-modified SiMS, SiMS@FeNP5, SiMS@FeNP5@SiO_2, SiMS@FeNP5@SiO_2@CdTe, pure FeNPs and TA-modified CdTe QDs. It can be seen that the significant peaks for SiMS are 470, 800, 1103, and 1240 cm^{-1}, attributed to the characteristic absorption bands of the Si-O-Si stretching and the peak at 943 cm^{-1} representing Si–OH bonds [43]. The spectrum of the MPS-modified SiMS exhibits two bands in the ranges 2985−2825 and 2600−2550 cm^{-1}, attributed to C−H and S−H stretching, respectively[42]. The significant peaks at 584 cm^{-1} is clearly shown after the FeNPs assembled onto the surfaces of the MPS-modified SiMS, attributed to the vibration of Fe–O bonds. The weak absorption bands at 2600−2550 cm^{-1} appear after coating the SiO_2/MPS layer as a buffer layer [44]. However, the stretching vibration of the thiol group disappeared with appearance of peaks at 1629 and 1419 cm^{-1} after immobilizing CdTe QDs onto the surface of these functional CPs, attributed to carboxyl stretching vibration and methylene scissoring vibration of TA components capped on the surface of CdTe QDs, respectively [45].

Figure 2a and 2b display the UV-vis and PL spectra of SiMS, SiMS@FeNP5, SiMS@FeNP5@SiO_2, SiMS@FeNP5@SiO_2@CdTe, pure FeNPs and CdTe QDs,

respectively. The absorption spectrum of SiMS@FeNP5 appears a broad absorption signal ranging from 330 nm to 550 nm, consistent with the absorption peak of FeNPs. (Figure 2a) The results suggest that assembled FeNPs with Fe–O–Si and Fe-S bonds sufficiently remained the original property of FeNPs [46]. A absorption peak at 603 nm appeared after immobilizing the CdTe onto the SiMS@FeNP5@SiO_2 surface, consistent with the absorption peak of pure CdTe QDs. Moreover, SiMS@FeNP5@SiO_2@CdTe exhibited a maximum emission wavelength at 651 nm. (Figure 2b) Compared with pure CdTe QDs, immobilizing the CdTe QDs onto the SiMS@FeNP5@SiO_2 surface led to ca. 13 nm of red-shift because of slight aggregation of CdTe QDs. Notable, the SiO_2 layer provides a buffer between FeNPs and CdTe QDs to prevent the quenching effect [47, 48]. XRD patterns of the as-synthesized samples are shown in Figure 2c. It can be observed a broad signal in the range of 2θ values between 16.5° and 33.2°, a typical characteristic in the XRD pattern of amorphous silica. The appearance of several sharp diffraction peaks (lattice planes) are observed at the 2θ values of 30.2°□(220), 35.8° (311), 43.3° (400), 57.1° (511), and 62.3° (440) after assembling FeNPs onto the SiMS, these peaks match well with standard Fe_3O_4 (JCPDS No. 88-0866) in face-centered-cubic phase. The nanocrystal structure of assembled FeNPs onto the SiMS surface is remained sufficiently. The pattern of SiMS@FeNP5@SiO_2@CdTe exhibits three extra

diffraction peaks (lattice planes) at the 2θ values of 25.6°(111), 40.2°(220) and 47.2°(311) consistent with the cubic structure of CdTe QDs (JCPDS No. 65-1046). According to the lattice plane (311) of Fe_3O_4 and (111) of CdTe and the, 15.2 nm and 7.3 nm of their nanocrystal sizes could be obtained, respectively, by calculating with Scherrer equation [49].

Figure 3a shows the typical magnetization curves of FeNPs, SiMS, SiMS@FeNP5, SiMS@FeNP5@SiO_2, and SiMS@FeNP5@SiO_2@CdTe at 298 K. The saturation magnetizations of FeNPs, SiMS@FeNP5, SiMS@FeNP5@SiO_2, and SiMS@FeNP5@SiO_2@CdTe were 66.3, 39.4, 33.8, and 30.5 emu g^{-1}, respectively. Although the saturation magnetizations of these CPs were smaller than that of pure FeNPs, weight ratios of the FeNPs to these CPs was extremely low (below 0.2 wt%). The saturation magnetizations of these particles were examined in dry state. In general, FeNPs may aggregate in dry state due to hydroxyl groups of the surface. The FeNPs assembled on the CPs could remain their dispersing without serious aggregation in dry state. On the other hand, nonmagnetic 3-μm SiMS could possess highly efficient magnetic behavior by assembling FeNPs as shell on the surfaces. Note that the saturation magnetization decreased slightly after modifying the SiMS@FeNP5 with SiO_2 layer and CdTe QDs, because of the increase in the content of nonmagnetic materials. The inset shows the hysteresis loops of these CPs, indicated

that all of the CPs exhibited typical superparamagnetic behavior. Pure FeNPs display a slight magnetic hysteresis, because of the aggregation of FeNPs in dry state. Moreover, Figure 3b illustrates the magnetic separation and redispersion process of the SiMS@FeNP5@SiO_2@CdTe CPs under normal light and 365 nm excitation. In absence of an external magnetic field, the solution of the as-synthesized the SiMS@FeNP5@SiO_2@CdTe CPs is brown and red under both normal light and UV irradiation in the aqueous solution. When a magnetic field (permanent magnet, 0.48T) is placed near the solution for 5 s, the CPs are attracted and accumulated toward the magnet, and the bulk solution becomes a clear phase, indicating that magnetic separation occurs. After the magnet was removed and followed by vigorous stirring, the aggregated CPs were quickly redispersed in water. These results suggest that our CPs can find potential applications in magnetic guiding and separation.

Figure 4 displays the SEM images of these CPs. Bare SiMS (diameter: 3 μm) had smooth spherical surfaces (Figure 4a). After modifying the silica surface with MPS, a thin-film–like layer appeared on the surface with presence of C (11.62%) and S (1.28%) atoms, obtained from EDX analysis (Figure 4b). For the SiMS@FeNPs CPs, we observed an increasingly pebble-like appearance upon increasing the FeNPs layers on the surface, suggesting that the coverage of FeNPs increased gradually on the SiMS surface (Figures 4c–4e). The surface roughness of the particles decreased

abruptly after assembled the TEOS/MPS layer onto the shell surface of SiMP@FeNP5 with presence of C (13.24%) and S (0.96 %) atoms (Figure 4f). The pebble-like structure reappeared after immobilizing CdTe QDS onto the SiMS@FeNP5@SiO_2 CPs with presence of Cd (0.46%) and Te (0.26 %) atoms (Figure 4g). Figure 5 presents TEM images of MPS-modified SiMS, SiMS@FeNP1, SiMS@FeNP3, SiMS@FeNP5, SiMS@FeNP5@SiO_2@CdTe. Relative to structure of the bare SiMS, a semi-transparent thin film (ca. 5 nm) surrounded them after treatment with MPS (Figure 5b). Thicker layers of FeNPs gradually formed as a shell structure upon increasing the cycles of LbL assembly of FeNPs (Figures 5b–d). We calculated shell thicknesses of 16 ± 8, 27 ± 8, and 45 ± 8 nm for SiMS@FeNP1, SiMS@FeNP3, and SiMS@FeNP5, respectively, using Gatan Digital Micrograph software. The satellite-like distribution [50] of CdTe QDs were clearly observed upon the SiO_2/MPS layer for the SiMs@FeNP5@SiO_2@CdTe (Figure 5e). The thickness of the SiO_2/MPS layer was approximately 20-30 nm, and average size of the QDs was ca. 7-10 nm (Figure 5f insert). In addition, Figure 5f displays the high resolution TEM (HRTEM) of FeNPs and CdTe layer upon the CPs. The lattice fringes with d-spacing was ca. 0.294 nm, consistent with the (220) lattice planes of Fe_3O_4 (Figure 5f left). The selected area electron diffraction (SAED) pattern in the Figure 5f inset represents the feature of FeNPs [51]. The lattice fringes with d-spacing of 0.361 nm correspond

to the (111) lattice planes of CdTe QDs.

We examined the superparamagnetic and highly efficient luminescence of the CPs with the TSDSC by a particle chaining behavior in the presence of an AMF. Figure 6 presents top-view optical microscopy (OM) images, parallel to the AMF, of the TSDSC encapsulating aqueous solutions of CPs (5.8 wt%) in the absence (left) and presence (right) of an AMF (field strength: ca. 87.5 gauss; frequency: 980 Hz). Because bare SiMS were non-magnetized, these particles remained their original status after applying the AMF (Figure 6a). SiMS@FeNPs were strung together in a line to form darker particles, resulting in the increase of open area in the TSDSC. Figures 6b–d reveal that number of darker SiMS@FeNPs CPs and open area of the TSDSC increased simultaneously with the FeNPs layers. Interestingly, the open area for SiMS@FeNPs CPs was increased significantly under the AMF, indicated that coating SiO_2/MPS layers onto the SiMS@FeNPs CPs enhanced the particle chaining behavior (Figure 6e). The presence of SiO_2/MPS layers provided the spacing among the CPs to avoid the random aggregation under the AMF. The open area did not change significantly for SiMS@FeNP5@SiO_2@CdTe due to nonmagnetic CdTe QDs (Figure 6f). Using Image-Pro Plus software (Media Cybernetics), we counted the number of particles per area ($170 \times 130\ \mu m^2$) directly from the top-view images of the TSDSC. We set the concentration of the testing suspension at 1.72×10^8 particles

mL^{-1} in each case. Moreover, we defined a chaining ratio (CR) to express the degree of particle chain formation in the TSDSC window, and calculated the open area ratio (OARs) to accurately describe the performance of the TSDSC.[52] Table 1 lists the CRs, OARs and contrast for all samples in the dispersing and chaining states. The CRs increased gradually from 0 to 69.23% upon increasing the FeNPs shell to five layers. CRs reached to ca. 82 and 88.46% for SiMS@FeNP5@SiO_2 and SiMS@FeNP5@SiO_2@CdTe, respectively. The results suggest that both of layer number of FeNPs and the buffer layer are the important factors to enhance the particle chaining behavior. Contrasts of the TSDSCs, defined as the difference of OARs between dispersing and chaining state, reached to 63.7 and 66.7 % for SiMS@FeNP5 and SiMS@FeNP5@SiO_2@CdTe CPs, respectively. Moreover, transmittances of the TSDSCs in the dispersing and chaining states at a wavelength of 550 nm for all samples were also recorded in the Figure 6g. The transmittance change from dispersing to chaining state for SiMS@FeNP5@SiO_2@CdTe CPs reached to 66.2 %, closed to the difference of OAR. The magneto-responsive transmittance could be reversible for 20 cycles at least, indicated that core/shell/satellite structured CPs, immobilized on the surfaces by covalent bonds, were stable. In addition, CLSM was exploited to observed the magneto-responsive luminescence in aqueous solutions with three-dimensional (3D) images. Figure 7a represents the top- (XY plane) and

side-view (XZ and YZ plane) CLSM images for SiMS@FeNP5@SiO_2@CdTe CPs in the absence of AMF. Apparent red luminescence in the Figure 7a represent the well-dispersed CPs in the TSDSC with low OAR (XY plane image). The CPs precipitated to stack obviously upon the bottom of TSDSC in the absence of AMF (XZ and YZ planes of side-view image). In the presence of AMF, the OAR increased significantly due to the particle chaining behavior (XY plane image in Figure 7b). The suspended CP chains in the aqueous solution without precipitation could be seen clearly in the XZ and YZ plane images. The results suggest that the precipitated CPs upon the bottom of TSDSC can be driven to suspend and chain linearly in the aqueous solution with an AMF.

Figure 8a displays the dependence of the transmittance at a wavelength of 550 nm in the presence of AMFs with various frequency from 1 to 4000 Hz. Transmittances of the TSDSCs increased abruptly to a maximum value upon increasing the frequency to 980 Hz, but decreased slowly over 980 Hz for all CPs. The frequency corresponding to highest transmittance for individual sample did not shift significantly with number of the FeNPs layers, suggesting that assembling FeNPs as shells on the microspheres still remained the stable magnetic property. Therefore, 980 Hz of frequency was determined to generate the optimal formation of particle chains. Moreover, the aqueous solutions of SiMS@FeNP5@SiO_2 and

SiMS@FeNP5@SiO_2@CdTe could generate the highest transmittance among these CPs, consistent with the results of OM observation. In addition, the transmittances of the TSDSC increased approximately linearly upon increasing the magnetic field to 87.5 gauss, but reached plateaus between 87.5 and 107.2 G. (Figure 8b) However, the transmittance decreased abruptly with tuning field strength to 128.6 G. When the hydrodynamic resistance was less than the induced force of the AMF [53], the particles aggregated irregularly leading to precipitation of the particles. Therefore, the optimal field strength range of AMFs for manipulation of these CPs was between 87.5 and 107.2 G (applied current: 2.0–2.5 A). In the presence of AMF, particle chaining can be influenced by two different mechanisms including Néel relaxation and the Brownian relaxation [54, 55]. Néel relaxation is caused by the free and rapid rotation of the magnetic dipole moment inside the smaller nanoparticles; Brownian relaxation is that the reorientation of magnetic dipole is blocked inside the particles, on the other hand, the entire particles must physically rotate in the suspensions. It is the widely known that Néel and Brownian rotation is depending on the agility, size, and shape of the cluster [56]. Using Eqs. (1) we calculated the complex magnetic permeability and, thereby, evaluated the degrees of magnetization of the CPs in response to AMFs. The complex magnetic permeability can be divided to two parts: a real part (χ', in phase), representing the energy storage capability, and an imaginary part (χ'', out of phase),

symbolizing the magnetic energy loss; these components are related to the loss tangent [$\tan\delta = \chi''/(1 + \chi')$]. Figure 9a plots the real and imaginary parts of the complex magnetic permeability with respect to the frequency of the AMF having a field strength of 87.5 gauss for FeNPs and these CPs. The value of χ' remained at a plateau in the frequency range between 1 and 100 Hz under the AMF for FeNPs; it decreased abruptly, however, upon increasing the frequency beyond 200 Hz, indicating that the degree of magnetization of the FeNPs in response to the AMF had also decreased abruptly. The value of χ' reached close to zero when the frequency reached 10,000 Hz. For the CPs, the value of χ' remained at a plateau in the frequency range between 1 and 300 Hz, wider than that for FeNPs, under the AMF. The results indicate that the assembling FeNPs as shells could enhance energy storage capability and stability without Brownian rotation. In addition, the value of χ'' reached its maximum value at a frequency of approximately 700 Hz, indicating the maximum of the dissipative processes in the FeNPs or irreversible movement of the domain wall. The frequency corresponding to maximum value of χ'' shifted to 1200 Hz for the CPs. The results indicate that Néel relaxation for the assembled FeNPs layers on the CPs are retarded. The behavior of the magnetic dipole moments for the CPs was determined predominately by Néel relaxation under AMFs in the range of frequency from 0 to 10,000 Hz. When the frequency of the AMF was greater than 10,000 Hz, the

Néel rotation of magnetic dipole moment could not keep up with the frequency. The magnetodisplay was heating slightly above 10,000 Hz, which could be attributed to the aggregation of CPs. Moreover, the energy dissipation of the magnetic particles could be described in terms of the loss tangent (loss factor). The loss tangent followed a trend similar to that of the imaginary part for all samples, indicating the frequency limitation of Néel rotation [56].(Figure 9c) Note that the values of χ' and χ'' are also relative to the weight ratio of FeNPs to the CPs.

Moreover, we evaluated the response time of the change in transmittance under the AMF of 87.5 gauss at a frequency of 980 Hz. Figure 10a displays the transmittances of the TSDSC encapsulating the aqueous solutions of CPs in real-time over three stages: from 0 to 10 s in the absence of AMF, within 30 s of switching on the AMF having a field strength of 87.5 gauss and a frequency of 980 Hz and within 50 s of switching off the AMF. The transmittance of the TSDSC encapsulating aqueous solutions of SiMS@FeNP5, SiMS@FeNP5@SiO_2 and SiMS@FeNP5@SiO_2@CdTe increased instantly upon switching on the AMF. The transmittance of the SiMS@FeNP5@SiO_2@CdTe solution increased from ca. 14 to 77% instantly upon switching on the AMF within 5 s. In the presence of AMF, the transmittances of SiMS@FeNP5, SiMS@FeNP5@SiO_2 and SiMS@FeNP5@SiO_2@CdTe solutions remained stable at their plateaus within the

period from 5 to 40 s. For aqueous solutions of these CPs, the transmittance decreased abruptly—from 77 to 18%, slightly higher than the initial transmittance—immediately after switching off the AMF; during the next 50 s (40–90 s in real-time), their transmittance remained stable without sedimentation. The transmittances did not return to their initial transmittance completely after switching off the AMF within 50-s period. Note that precipitate of CPs occurred gradually after switching off the AMF, resulting in gradual decrease of the transmittance to approach their initial transmittance for ca. 3 hr. For SiMS@FeNP1 and SiMS@FeNP3 solutions, the response time to reach the maximum transmittances were approximately 24 and 22 s after switching on the AMF, respectively, due to lower weight ratio of FeNPs to the CPs. The transmittance also decreased immediately after switching off the AMF. These observations suggest that all CPs exhibit superparamagnetism in the solutions without residual magnetic dipole moment. The transmittance change for SiMS@FeNP5@SiO_2@CdTe solution reached over 73 %, which may meet the request for display application. Figure 10b displays photographs of the TSDSC encapsulating the aqueous suspension of SiMS@FeNP5@SiO_2@CdTe (5.8 wt%) in the absence of AMF under normal light and 365 nm excitation. The CPs were well-dispersed in the solution, resulting in a brown color (opaque) of the TSDSC (Figure 10b left). The pattern behind the TSDSC could not be recognized completely

by the naked eye because the dispersive particles blocked the normal light traveling through the TSDSC. In addition, the TSDSC exhibited red luminescence under 365 nm excitation (Figure 10b right). The pattern (NTUST's logo) could be clearly seen after applying the AMF (980 Hz and 87.5 gauss) for 10 s, indicating a significant increase in transmittance.(Figure 10c left) In addition, the particle chaining behavior resulted the increase of OAR in the presence of AMF. Intensity of red luminescence of the TSDSC decreased significantly from the top-viewing. (Figure 10c right) The results showed that the CPs displayed a strong red emission and superparamagnetic behavior at room temperature; therefore, the CPs is expected to find many potential applications in display fields.

Conclusion

We reported the synthesis of core/shell/satellite CPs with bifunctional magnetic-luminescent property. Superparamagnetism of FeNPs and luminescence of CdTe QDs are generally exhibited for nanoscale particles. Assembling napaericles as nanocrystal shells could endue these remarkable specific properties on microscale particles. A home-made TSDSC encapsulating with these aqueous solution of CPs exhibited significant change in transmittance and luminescence due to particle chaining behavior in presence of an AMF. Because of the superparamagnetism, the transmittance and luminescence of the TSDSC could be switched reversibly without

residual magnetic dipole. The as-prepared bifunctional CPs combined the advantages of superparamagnetism and luminescence, which will find extensive application in magnetodisplay. Many complex composite nanostructures with tailored functions can be efficiently produced by using this versatile approach.

Acknowledgment

We thank the Ministry of Science and Technology in the Republic of China for supporting this research financially.

References

[1] Caruso, F. Nanoengineering of Particle Surfaces, *Adv. Mater.* **2001**, *13*, 11–22.

[2] Fang, F.F.; Liu, Y.D.; Choi, H.J.; Seo, Y. Core–shell structured carbonyl ironmicrospheres prepared via dual-dtep functionality coatings and their magne-torheological response, *ACS Appl. Mater. Interfaces* **2011**, *3*, 3487–3495.

[3] Roca, M.; Haes, A. J. Silica−Void−Gold Nanoparticles: Temporally Stable Surface-Enhanced Raman Scattering Substrates, *J. Am. Chem. Soc.* **2008**, *130*, 14273–14279.

[4] Yi, D. K.; Lee, S. S.; Ying, J. Y. Synthesis and Applications of Magnetic Nanocomposite Catalysts, *Chem. Mater.* **2006**, *18*, 2459–2461.

[5] Feng, X.; Mao, C.; Yang, G.; Hou,W.; Zhu, J. J. Polyaniline/Au Composite Hollow Spheres: Synthesis, Characterization, and Application to the Detection of Dopamine, *Langmuir* **2006**, *22*, 4384–4389.

[6] Salgueirio-Maceira, V.; Correa-Duarte, M. A.; Spasova, M.; Liz-Marz an, L. M.; Farle, M. Composite Silica Spheres with Magnetic and Luminescent Functionalities, *Adv. Funct. Mater.* **2006**, *16*, 509–514.

[7] Mangeney, C.; Bousalem, S.; Connan, C.; Vaulay, M.; Bernard, S.; Chehimi, M. M. Latex and Hollow Particles of Reactive Polypyrrole: Preparation, Properties, and Decoration by Gold Nanospheres, *Langmuir* **2006**, *22*, 10163–10169.

[8] Ghosh Chaudhuri, R.; Paria, S., Core/Shell Nanoparticles: Classes, Properties, Synthesis Mechanisms, Characterization, and Applications. *Chem. Rev.* **2011,** *112* (4), 2373-2433.

[9] Radtchenko, I. L.; Sukhorukov, G. B.; Gaponik, N.; Kornowski, A.; Rogach, A. L.; Mo¨hwald, H. Core–Shell Structures Formed by the Solvent-Controlled Precipitation of Luminescent CdTe Nanocrystals on Latex Spheres, *Adv. Mater.* **2001**, *13*, 1684-1687.

[10] Decher, G. Fuzzy Nanoassemblies: Toward Layered Polymeric Multicomposites, *Science* **1997**, *277*, 1232-1237.

[11] Wang, Y.; Angelatos, A. S.; Caruso, F. Template Synthesis of Nanostructured Materials via Layer-by-Layer Assembly, *Chem. Mater.* **2008**, *20*, 848-858.

[12] Slowing, I. I.; Trewyn, B. G.; Giri, S.; Lin, V. S.-Y. Mesoporous Silica Nanoparticles for Drug Delivery and Biosensing Applications, *Adv. Funct. Mater.* **2007**, *17*, 1225−1236.

[13] Marlow, F.; Muldarisnur.; Sharifi, P.; Brinkmann, R.; Mendive, C. Opals: Status and Prospects, *Angew. Chem., Int. Ed.* **2009**, *48*, 6212−6233.

[14] Guerrero-Martínez, A.; Pérez-Juste, J.; Liz-Marzán, L. M. Recent Progress on Silica Coating of Nanoparticles and Related Nanomaterials, *Adv. Mater.* **2010**, *22*, 1182−1195.

[15] Zou, H.; Wu, S.; Shen, J. Polymer/Silica Nanocomposites: Preparation, Characterization, Properties, and Applications, *Chem. Rev.* **2008**, *108*, 3893−3957.

[16] Yathindranath, V.; Worden, M.; Sun, Z.; Miller, D. W.; Hegmann, T. A general synthesis of metal (Mn, Fe, Co, Ni, Cu, Zn) oxide and silica nanoparticles based on a low temperature reduction/hydrolysis pathway. *RSC Adv*. **2013**, *3*, 23722−23729.

[17] Wong, Y. J.; Zhu, L.; Teo, W. S.; Tan, Y. W.; Yang, Y.; Wang, C.; Chen, H. Revisiting the Stöber Method: Inhomogeneity in Silica Shells, *J. Am. Chem. Soc.* **2011**, *133*, 11422−11425.

[18] Kim, Y.J.; Liu, Y.D.; Seo, Y.; Choi, H.J.; Pickering-emulsion-polymerizedpolystyrene/Fe2O3composite particles and their magnetoresponsive charac-teristics, *Langmuir* **2013**, *29*, 4959–4965.

[19] Jing, L.; Yang, C.; Qiao, R.; Niu, M.; Du, M.; Wang, D.; Gao, M. Highly Fluorescent CdTe@SiO2 Particles Prepared via Reverse Microemulsion Method, *Chem. Mater.* **2010**, *22*, 420−427.

[20] Leng, W.; Chen, M.; Zhou, S.; Wu, L. Capillary Force Induced Formation of Monodisperse Polystyrene/Silica Organic−Inorganic Hybrid Hollow Spheres, *Langmuir* **2010**, *26*, 14271−14275.

[21] Qi, G.; Wang, Y.; Estevez, L.; Switzer, A. K.; Duan, X.; Yang, X.; Giannelis, E. P. Facile and Scalable Synthesis of Monodispersed Spherical Capsules with a

Mesoporous Shell, *Chem. Mater.* **2010**, *22*, 2693−2695.

[22] Hong, J.; Lee, J.; Rhymb, Y. M.; Kim, D. H.; Shim, S. E. Polyelectrolyte-assisted synthesis of polystyrene microspheres by dispersion polymerization and the subsequent formation of silica shell, *J. Colloid Interface Sci.* **2010**, *344*, 410−416.

[23] Li, C.-L.; Chen, J.-K.; Fan, S.-K.; Ko, F.-H.; Chang, F.-C., Electrorheological Operation of Low-/High-Permittivity Core/Shell SiO2/Au Nanoparticle Microspheres for Display Media. *ACS Appl. Mater. Interfaces* **2012,** *4* (10), 5650-5661.

[24] Sedlacik, M.; Moucka, R.; Kozakova, Z. Kazantseva, N. E.; Pavlinek, V.; Kuritka, I.; Kaman, O.; Peer, P. Correlation of structural and magnetic properties of Fe_3O_4 nanoparticles with their calorimetric and magnetorheological performance. *J. Magn. Magn. Mater.* **2013**, *326*, 7–13.

[25] Sedlacik, M.; Pavlinek, V. A tensiometric study of magnetorheological suspensions' stability. *RSC Adv*. **2014**, *4*, 58377–58385.

[26] Martin, B. R.; Dermody, D. J.; Reiss, B. D.; Fang, M. M.; Lyon, L. A.; Natan, M. J.; Mallouk, T. E. Orthogonal Self-Assembly on Colloidal Gold-Platinum Nanorods, *Adv. Mater.* **1999**, *11*, 1021–1025.

[27] Huo, L.; Li,W.; Lu, L.; Cui, H.; Xi, S.;Wang, J.; Zhao, B.; Shen, Y.; Lu, Z. Preparation, Structure, and Properties of Three-Dimensional Ordered α-Fe2O3 Nanoparticulate Film, *Chem. Mater.* **2000**, *12*, 790–794.

[28]Jun, Y.-W.; Lee, J.-H.; Cheon, J. Chemical design of nanoparticle probes for high-performance magnetic resonance imaging, *Angew. Chem., Int. Ed.* **2008**, *47*, 5122-5135.

[29] Suh, W. H.; Suh, Y.-H.; Stucky, G. D. Multifunctional nanosystems at the interface of physical and life sciences, *Nano Today* **2009**, *4*, 27-36.

[30] Liong, M.; Lu, J.; Kovochich, M.; Xia, T.; Ruehm, S. G.; Nel, A. E.; Tamanoi, F.; Zink, J. I. Multifunctional Inorganic Nanoparticles for Imaging, Targeting, and Drug Delivery, *ACS Nano* **2008**, *2*, 889-896.

[31] Koole, R.; Mulder, W. J. M.; van Schooneveld, M. M.; Strijkers, G. J.; Meijerink, A.; Nicolay, K. Magnetic quantum dots for multimodal imaging, *Wiley Interdiscip. Rev.: Nanomed. Nanobiotechnol.* **2009**, *1*, 475-491.

[32] Selvan, S. T.; Patra, P. K.; Ang, C. Y.; Ying, J. Y. Synthesis of Silica-Coated Semiconductor and Magnetic Quantum Dots and Their Use in the Imaging of Live Cells, *Angew. Chem., Int. Ed.* **2007**, *46*, 2448-2452.

[33] Kim, J.; Lee, J. E.; Lee, J.; Yu, J. H.; Kim, B. C.; An, K.; Hwang, Y.; Shin, C.-H.; Park, J.-G.; Kim, J.; Hyeon, T. Magnetic Fluorescent Delivery Vehicle Using Uniform Mesoporous Silica Spheres Embedded with Monodisperse Magnetic and Semiconductor Nanocrystals, *J. Am. Chem. Soc.* 2006, 128, 688-689.

[34] Haryono, A.; Binder, W. Controlled Arrangement of Nanoparticle Arrays in

Block-Copolymer Domains, *Small* **2006**, *2*, 600-611.

[35] Chen, J.-K.; Qui, J.-Q. Nanowires of 3-D cross-linked gold nanoparticle assemblies behave as thermosensors on silicon substrates. *Colloid Polym. Sci.* **2011**, *289* (17), 1829–1837.

[36] T. Ukai, T. Maekawa, Patterns formed by paramagnetic particles in a horizontallayer of a magnetorheological fluid subjected to a DC magnetic field, *Phys. Rev. E* **2004**, *69*, 032501.

[37] M. Sedlacik, V. Pavlinek, P. Peer, P. Filip, Tailoring the magnetic properties and magnetorheological behavior of spinel nanocrystalline cobalt ferrite by varying annealing temperature, *Dalton Trans*. **2014**, *43*, 6919–6924.

[38] Caregnato, P.; Forbes, M. D. E.; Soria, D. B.; Mártire, D. O.; Gonzalez, M. n. C., Chemisorbed Thiols on Silica Particles: Characterization of Reactive Sulfur Species. *J. Phys. Chem. C* **2010,** *114* (11), 5080-5087.

[39] Dong, A.; Lan, S.; Huang, J.; Wang, T.; Zhao, T.; Xiao, L.; Wang, W.; Zheng, X.; Liu, F.; Gao, G.; Chen, Y., Modifying Fe3O4-Functionalized Nanoparticles with N-Halamine and Their Magnetic/Antibacterial Properties. *ACS Appl.Mater. Interfaces* **2011,** *3* (11), 4228-4235.

[40] Chen, J.-K.; Qui, J.-Q., Patterned 3D Assembly of Au Nanoparticle on Silicon Substrate by Colloid Lithography, *J. Nanopart. Res.* **2012,** *14*, 942-956.

[41] Erez, N.; Gordon, G.; Nest, M.; Kurizki, G. Thermodynamic control by frequent quantum measurements, *Nature* **2008**, *452*, 724–727.

[42] Li, C.; Chang, C.; Chen, J. Fabrication of of Sandwich Structured Devices Encapsulating Core/Shell SiO_2/Fe_3O_4 Nanoparticle Microspheres as Media for Magneto-responsive Transmittance, *Sens. Actuators B: Chem* **2015**, 210, 46–55.

[43] Fleming, M. S.; Mandal, T. K.; Walt, D. R., Nanosphere−Microsphere Assembly: Methods for Core−Shell Materials Preparation. *Chem. Mater.* **2001,** *13* (6), 2210-2216.

[44] Lu, Z.; Gao, C.; Zhang, Q.; Chi, M.; Howe, J. Y.; Yin, Y., Direct Assembly of Hydrophobic Nanoparticles to Multifunctional Structures. *Nano Lett.* **2011,** *11* (8), 3404-3412.

[45] Liu, J.; Zhang, Y.; Yan, C.; Wang, C.; Xu, R.; Gu, N., Synthesis of Magnetic/Luminescent Alginate-Templated Composite Microparticles with Temperature-Dependent Photoluminescence under High-Frequency Magnetic Field. *Langmuir* **2010,** *26* (24), 19066-19072.

[46] Hui, C.; Shen, C.; Tian, J.; Bao, L.; Ding, H.; Li, C.; Tian, Y.; Shi, X.; Gao, H.-J., Core-shell $Fe_3O_4@SiO_2$ nanoparticles synthesized with well-dispersed hydrophilic Fe_3O_4 seeds. *Nanoscale* **2011,** *3* (2), 701-705.

[47] Corr, S.; Rakovich, Y.; Gun'ko, Y. Multifunctional Magnetic-fluorescent

Nanocomposites for Biomedical Applications. *Nanoscale Res. Lett.* **2008,** *3* (3), 87-104.

[48] Anup, K.; Sonia, K.; Prasad, Y.; Haribhau, G.; Renu, P.; Jog, J. P.; Benoit, L.; Béatrice, H.; Padma, S.; Satishchandra, O., Magnetite/CdTe magnetic–fluorescent composite nanosystem for magnetic separation and bio-imaging. *Nanotechnology* **2011,** *22* (22), 225101.

[49] Patterson, A. L. The Scherrer Formula for X-Ray Particle Size Determination. *Phys. Rev.* **1939,** *56* (10), 978-982.

[50] Chen, T.-H.; Jean, R.-D.; Chiu, K.-C.; Chen, C.-H.; Liu, D.-M., Transparent SiO2-Ag core-satellite nanoparticle assembled layer for plasmonic-based chemical sensors. *Applied Physics Letters* **2012,** *100* (22), 223101.

[51] Xia, H.; Cheng, D.; Xiao, C.; Chan, H. S. O., Controlled synthesis of polyaniline nanostructures with junctions using in situ self-assembly of magnetic nanoparticles. *J. Mater. Chem.* **2005,** *15* (38), 4161-4166.

[52] Li, C.; Chang, C.; Chen, J. Fabrication of of Sandwich Structured Devices Encapsulating Core/Shell SiO_2/Fe_3O_4 Nanoparticle Microspheres as Media for Magneto-responsive Transmittance, *Sens. Actuators B: Chem* **2015**, 210, 46–55.

[53] K. van Netten, J. Zhou, K.P. Galvin, R. Moreno-Atanasio, Influence of magneticand hydrodynamic forces on chain-aggregation and motion of

magnetisableparticles and composites, *Chem. Eng. Sci.* **2013,** *93*, 229–237.

[54] Néel, L. Some theoretical aspects of rock-magnetism. *Adv. Phys.* **1955,** *4* (14), 191-243.

[55] de la Presa, P.; Luengo, Y.; Multigner, M.; Costo, R.; Morales, M. P.; Rivero, G.; Hernando, A., Study of Heating Efficiency as a Function of Concentration, Size, and Applied Field in γ-Fe_2O_3 Nanoparticles. *J. Phys. Chem. C* **2012,** *116* (48), 25602-25610.

[56] Erné, B. H.; Butter, K.; Kuipers, B. W. M.; Vroege, G. J., Rotational Diffusion in Iron Ferrofluids. *Langmuir* **2003,** *19* (20), 8218-8225.

Figure captions

Figure 1: FTIR spectra of SiMS, MPS-modified SiMS, SiMS@FeNP5, SiMS@FeNP5@SiO_2, SiMS@FeNP5@SiO_2@CdTe, pure FeNPs and TA-modified CdTe QDs.

Figure 2: (a) UV-vis, (b) PL spectra and (c) XRD patterns of SiMS, SiMS@FeNP5, SiMS@FeNP5@SiO_2, SiMS@FeNP5@SiO_2@CdTe, FeNPs and CdTe QDs.

Figure 3: (a) Magnetization curves, measured using a SQUID at room temperature, of FeNPs, SiMS, SiMS@FeNP5, SiMS@FeNP5@SiO_2, and SiMS@FeNP5@SiO_2@CdTe. (b) Photographs of aqueous solutions of the as-synthesized SiMS@FeNP5@SiO_2@CdTe CPs in the absence and presence of a permanent magnet (0.48T) under normal light and UV irradiation.

Figure 4: SEM images of (a) SiMS, (b) MPS-modified SiMS, (c) SiMS@FeNP1, (d) SiMS@FeNP3, (e) SiMS@FeNP5, (f) SiMS@FeNP5@SiO_2, (g) SiMS@FeNP5@SiO_2@CdTe.

Figure 5: TEM images of (a) MPS-modified SiMS, (b)SiMS@FeNP1, (c)SiMS@FeNP3, (d) SiMS@FeNP5 and (e)SiMS@FeNP5@SiO_2@CdTe. (f)HRTEM of (e), assembled FeNPs layers of the inner shells (left, insert is SAED pattern) and CdTe QDs layer of the outer shell (right).

Figure 6: OM images of aqueous solutions (5.8 wt%) of (a) SiMS, (b) SiMS@FeNP1, (c) SiMS@FeNP3, (d) SiMS@FeNP5, (e) SiMS@FeNP5@SiO_2, and (f) SiMS@FeNP5@SiO_2@CdTe in the absence (left) and presence (right) of AMF (frequency: 980 Hz, strength: 87.5 gauss). (g) Transmittances at a wavelength of 550 nm of TSDSC (thickness: 100 μm) encapsulating aqueous solutions of these CPs in the absence and presence of AMF.

Figure 7: CLSM images including XY (middle; top-view), XZ (below, side-view) and YZ (right, side-view) plane images of the TSDSC encapsulating aqueous solutions of the as-synthesized SiMS@FeNP5@SiO_2@CdTe in the (a) absence and (b) presence of AMF.

Figure 8: Transmittances of TSDSC encapsulating aqueous solutions of these CPs in the presence of AMF, plotted with respect to (a) the field frequency from 1-4000 Hz at the field strength 87.5 gauss and (b) the field strength from 0-128.6 gauss at the frequency 980 Hz.

Figure 9: (a) Real (μ'), (b) imaginary (μ") parts of complex magnetic permeability and loss tangent (tanδ) of SiMS, SiMS@FeNP1, SiMS@FeNP3, SiMS@FeNP5, SiMS@FeNP5@SiO_2, SiMs@FeNP5@SiO_2@CdTe, and pure FeNPs plotted with respect to the frequency of the AMF.

Figure 10: (a) Transmittance of TSDSC encapsulating aqueous solutions of these CPs

in real-time over three stages: from 0 to 10 s in the absence of AMF, within 30 s of switching on the AMF having a field strength of 87.5 gauss and a frequency of 980 Hz and within 50 s of switching off the AMF. (b) Photographs of TSDSC encapsulating aqueous solution of SiMS@FeNP5@SiO_2@CdTe in the (b) absence and (c) presence of AMF (frequency: 980 Hz, field strength: 87.5 gauss) for 10 s under normal light (left) and UV irradiation (right).

Scheme 1. Schematic representation of preparation of core/shell/satellite structured SiMS@FeNPs@SiO_2@CdTe CPs.

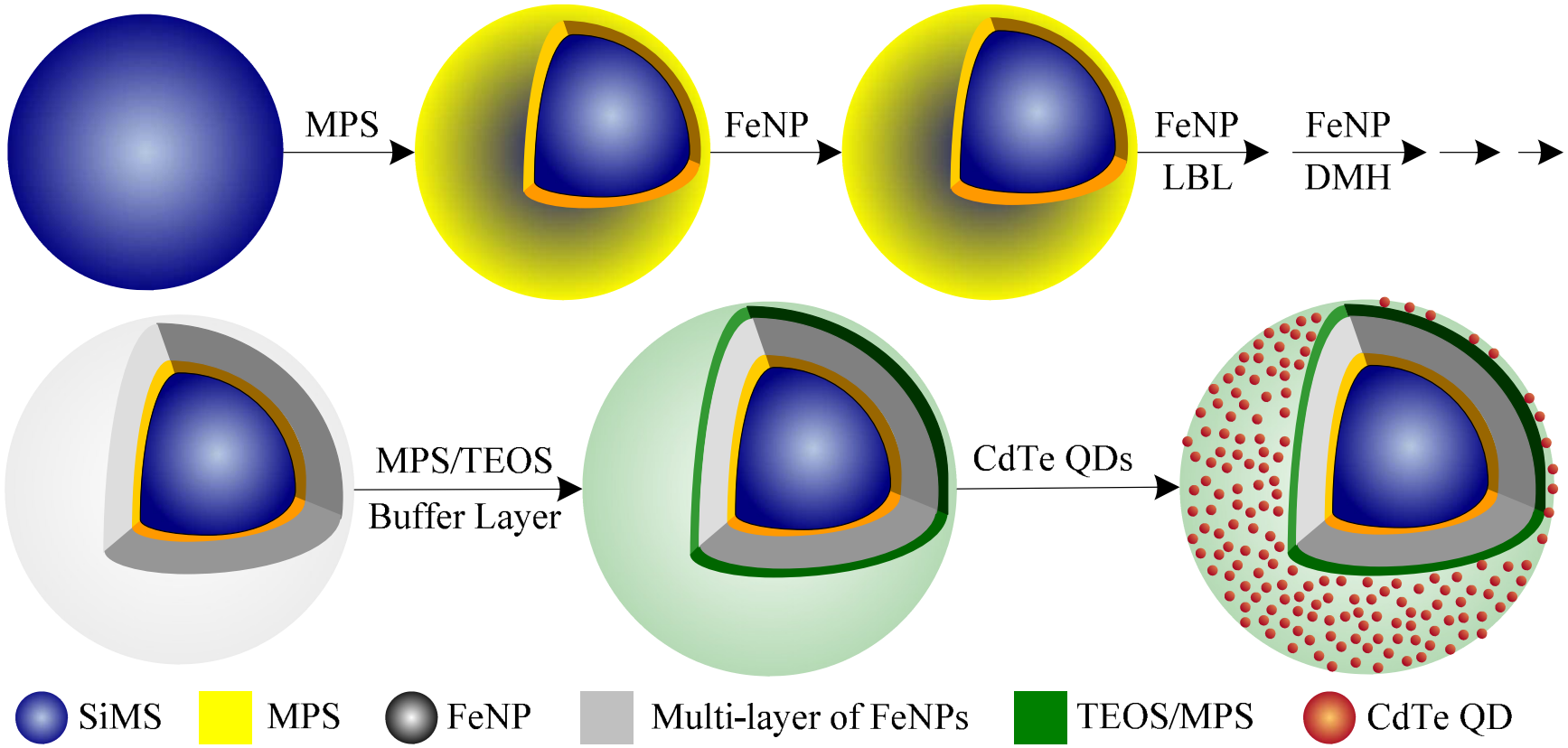

Scheme 2 Cartoon representations of TSDSC, fabricated with a Teflon layer and spacer coating onto two acrylic plates, placed into a solenoid coil, in the dispersing state (the CPs dispersed randomly in the suspension) and the chaining state (the CPs polarized by applying an AMF, resulting in the formation of particle chains).

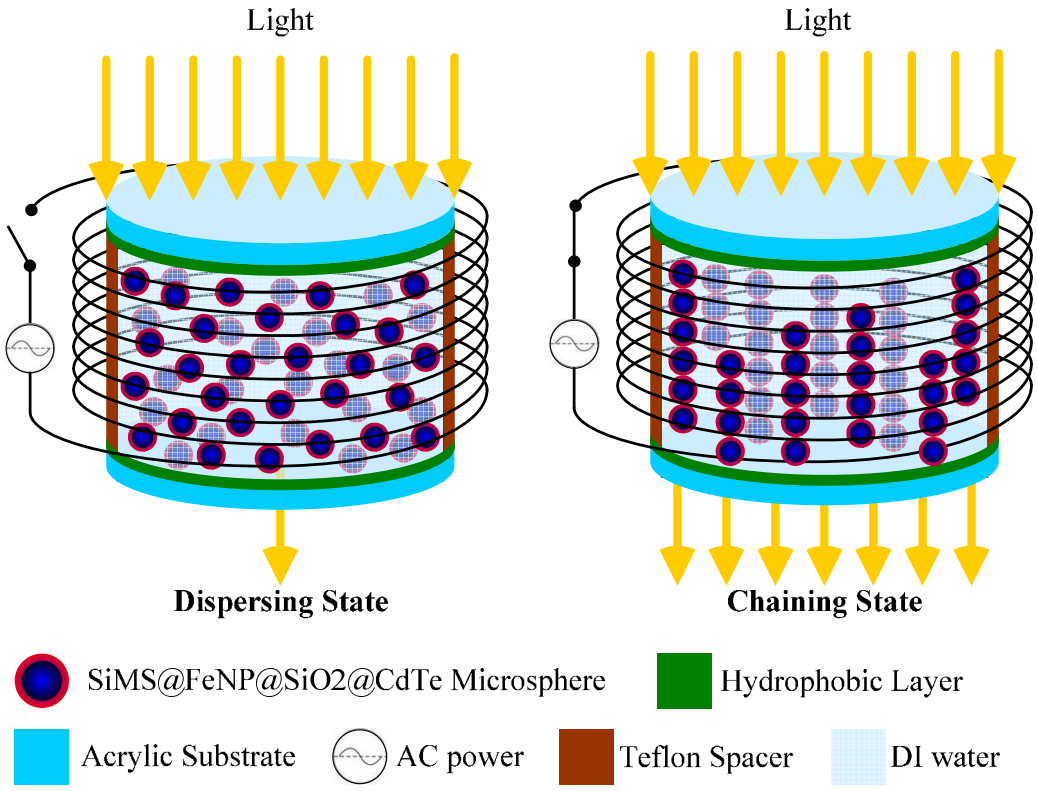

Table 1 Number of the particles, CRs, OARs and contrast determined from top-view OM images in dispersing and chaining states

Particle	Particle Counts[a]		CR[d] (%)	OAR[e](%)		Contrast[f] (%)
	Dispersing state[b]	Chaining state[c]		Dispersing state[b]	Chaining state[c]	
SiMS	2700 ± 100	2700 ± 100	0	0.8	0.8	0
SiMS@FeNP1	2500 ± 100	2100 ± 100	16.00 ± 0.04	0.9	31.5	30.6
SiMS@FeNP3	2700 ± 100	1600 ± 100	40.74 ± 0.04	1.1	46.7	45.6
SiMS@FeNP5	2600 ± 100	800 ± 100	69.23 ± 0.04	0.9	64.6	63.7
SiMS@FeNP5@SiO_2	2500 ± 100	450 ± 100	82.00 ± 0.04	1.1	67.3	66.2
SiMS@FeNP5@SiO_2@CdTe	2600 ± 100	300 ± 100	88.46 ± 0.04	0.8	67.5	66.7

[a] Number of particles counted directly by Image Pro Plus software from top-view images over an area of 170×130 μm^2.

[b] Original state of TSDSC in the absence of magnetic fields.

[c] An AMF with 87.5 gauss of field strength and 980 Hz of frequency was applied on the TSDSC.

[d] Chaining ratio (CR) $= \frac{N - N_p}{N} \times 100\%$, where N and Np the number of particles directly counted in top-view images recorded in dispersing and chaining states, respectively.

[e] Open area ratio (OAR) is defined as $\left(1 - \frac{A_m}{A}\right) \times 100\%$, where A and A_m represent the total area of the TSDSC and the area of isolated chained particles, respectively, as measured from top-view images.

[f] Contrast = difference of OAR in the dispersing and chaining state.

Figure 1

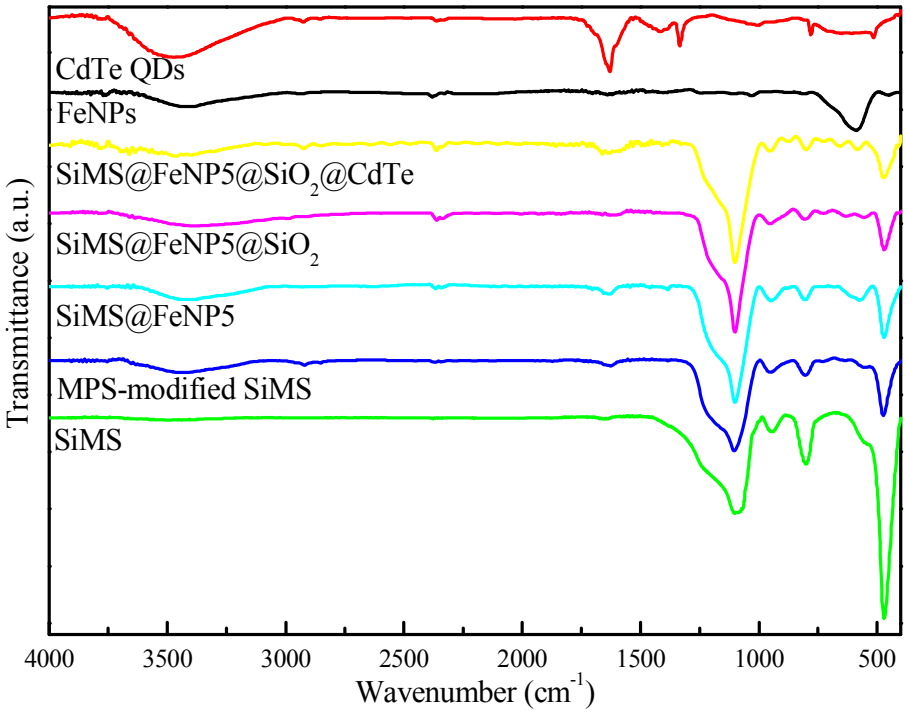

Figure 2

(a)

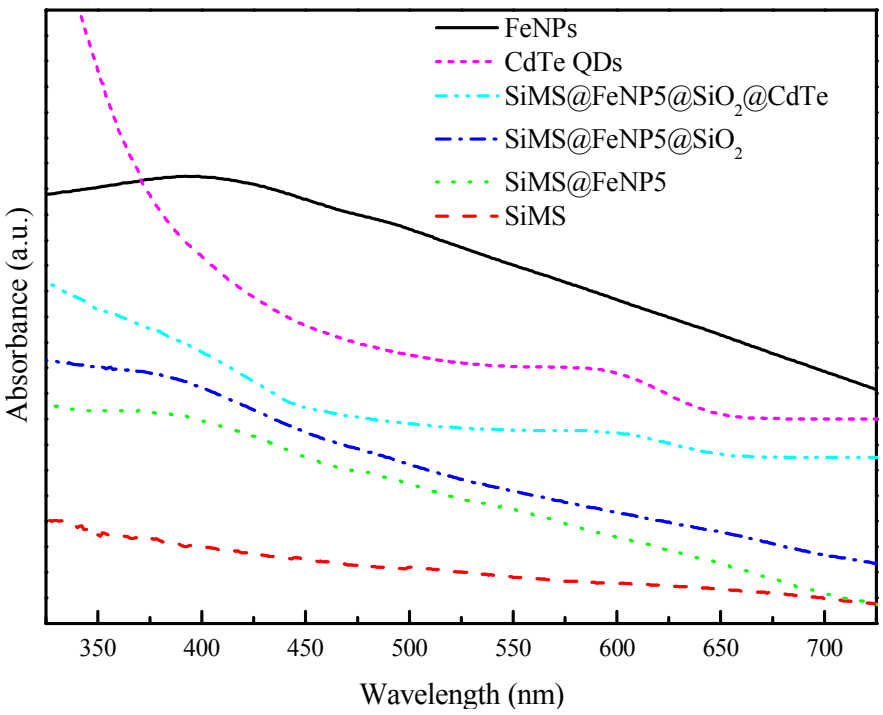

(b)

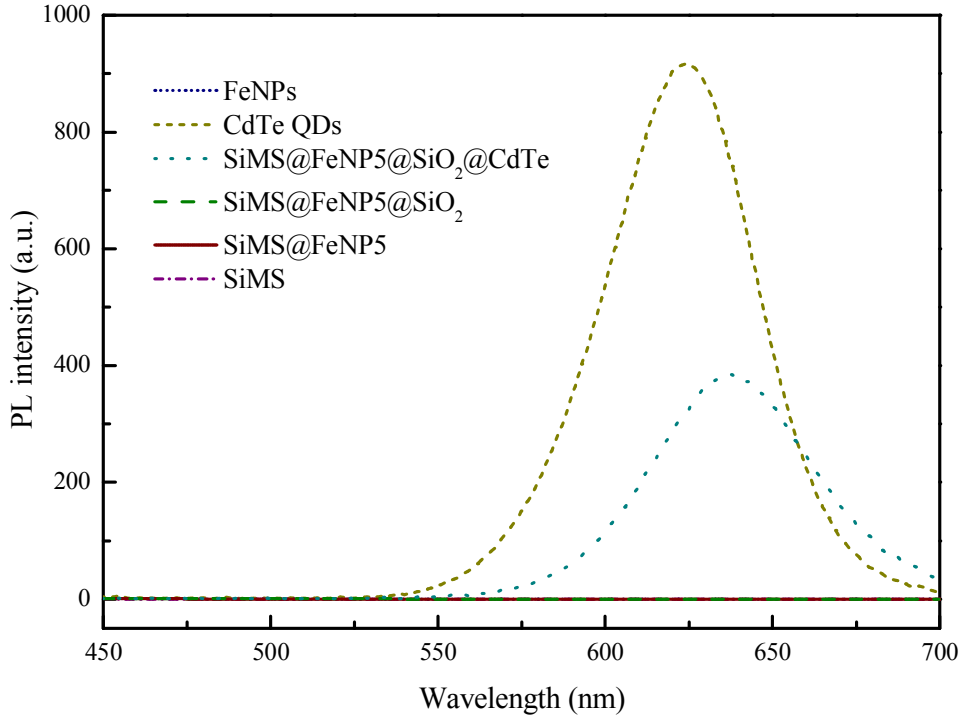

(c)

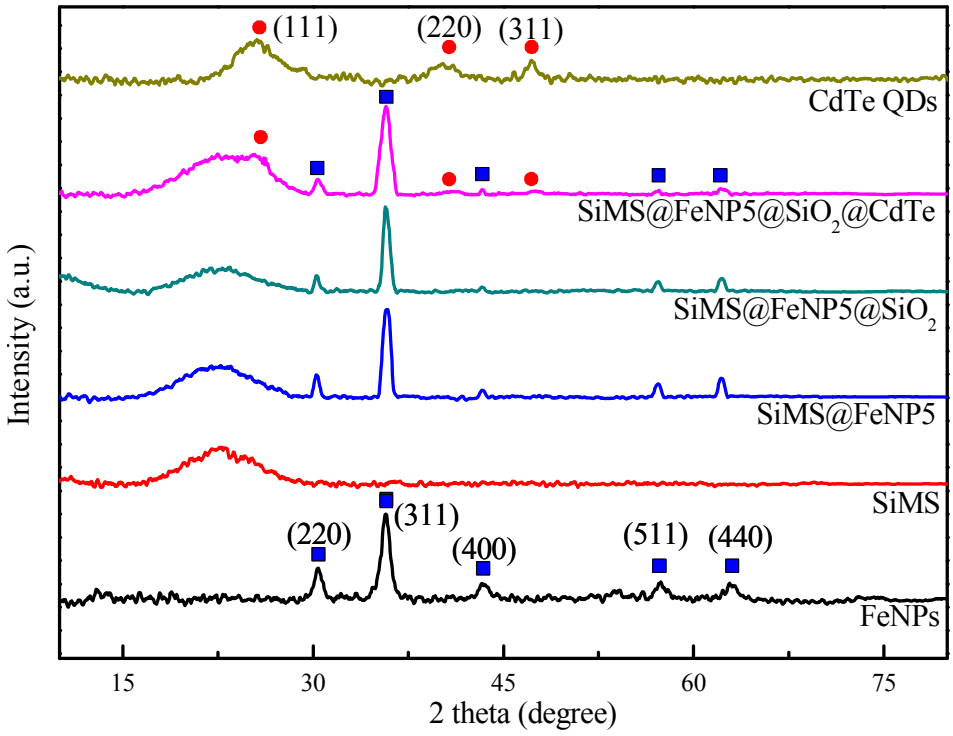

Figure 3

(a)

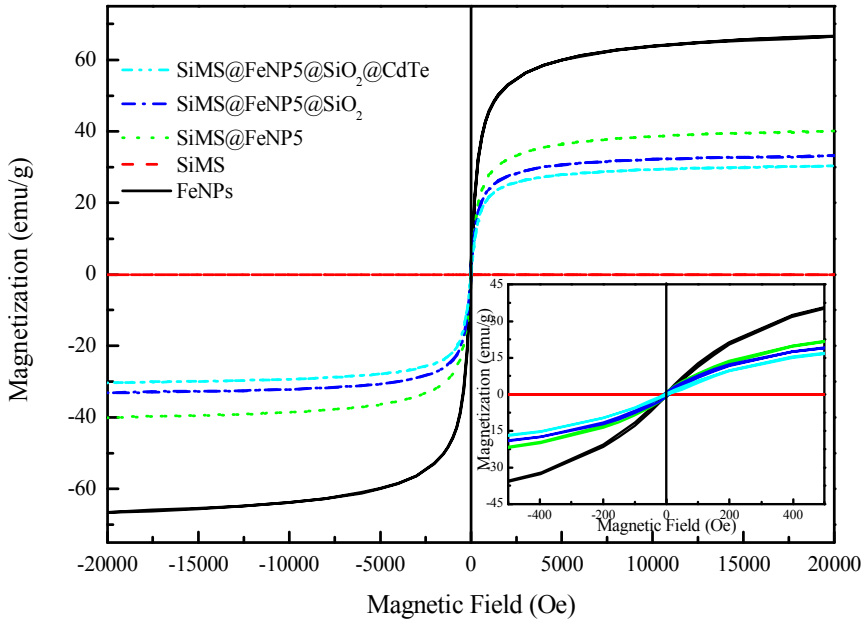

(b)

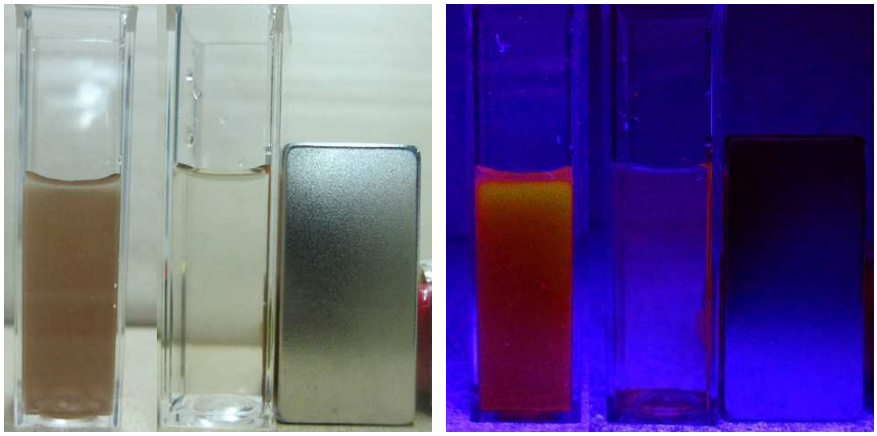

Figure 4
(a)

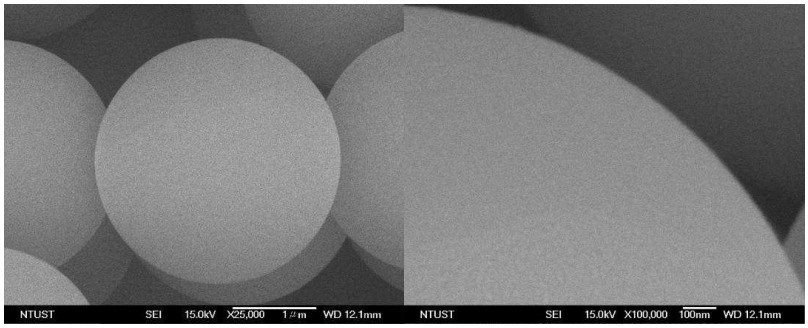

(b)

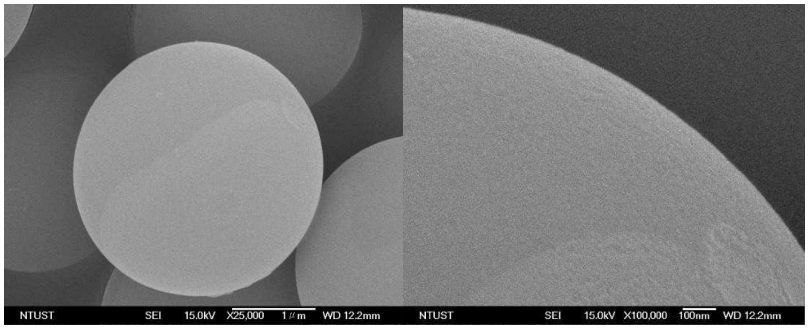

(c)

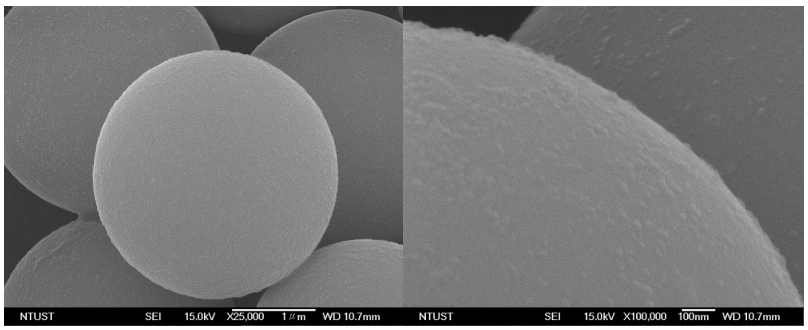

(d)

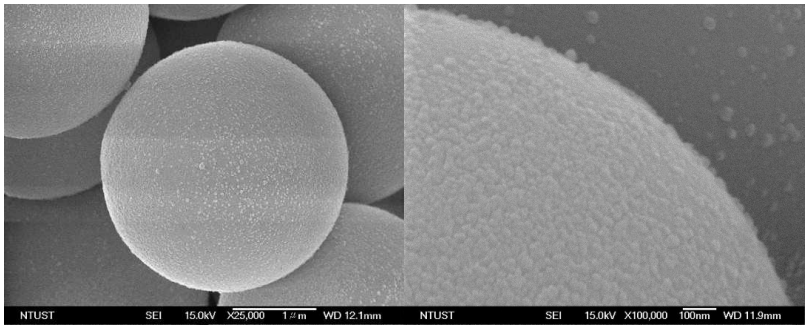

(e)

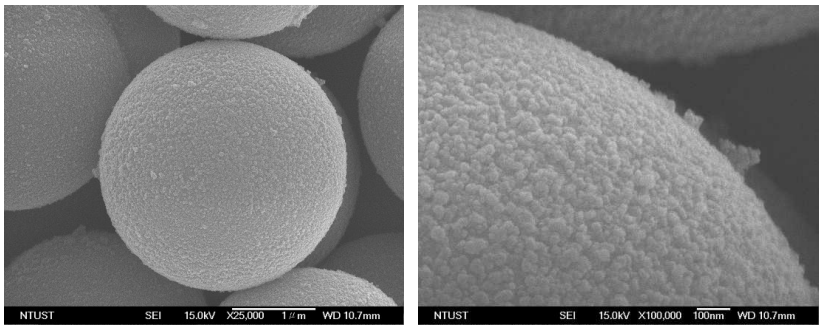

(f)

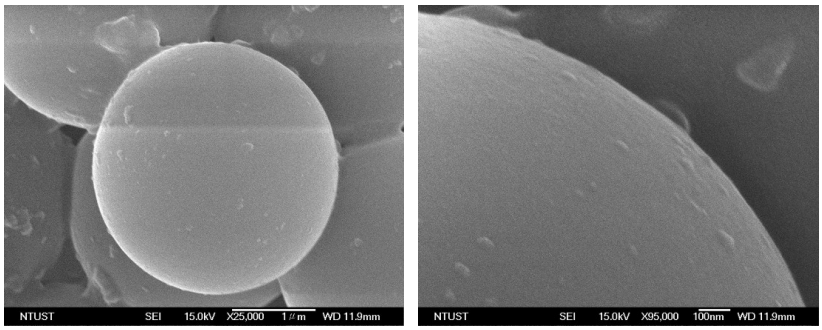

(g)

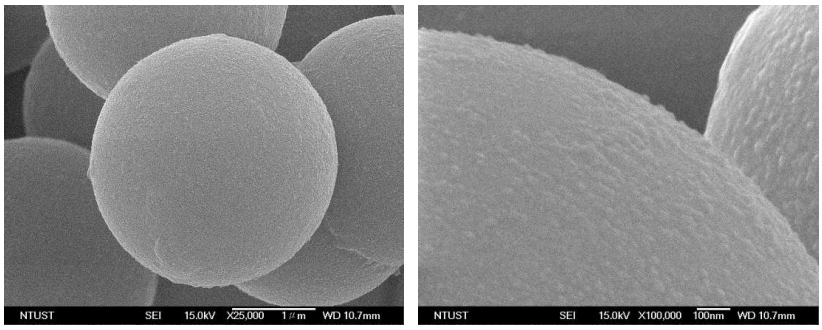

Figure 5

(a)

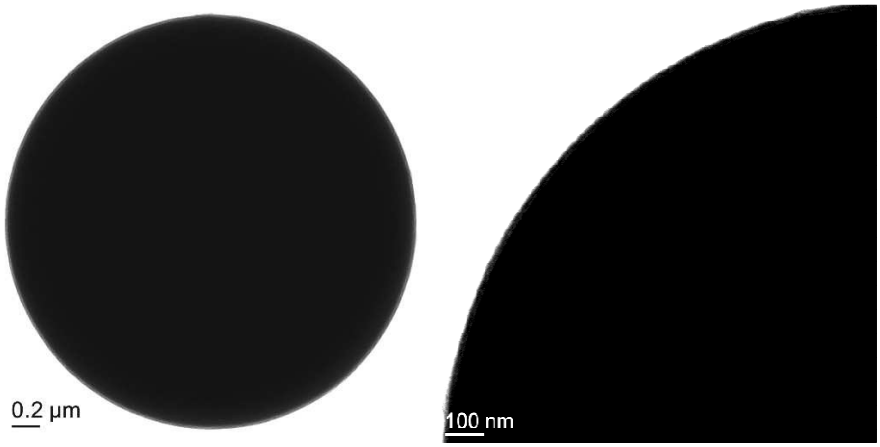

(b)

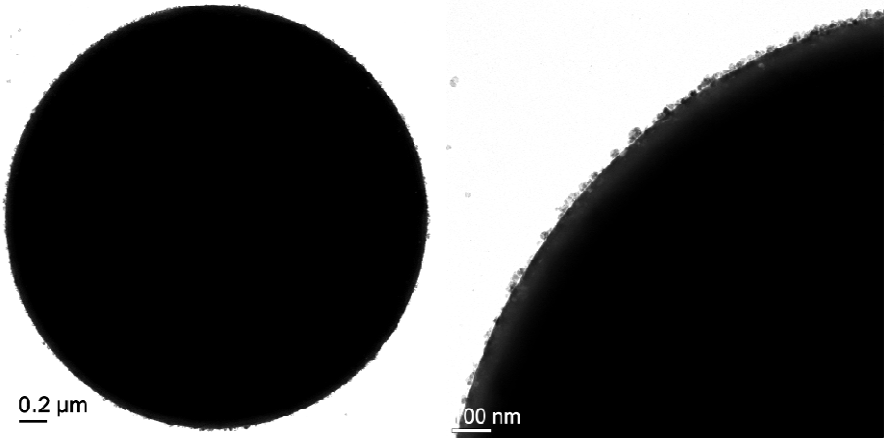

(c)

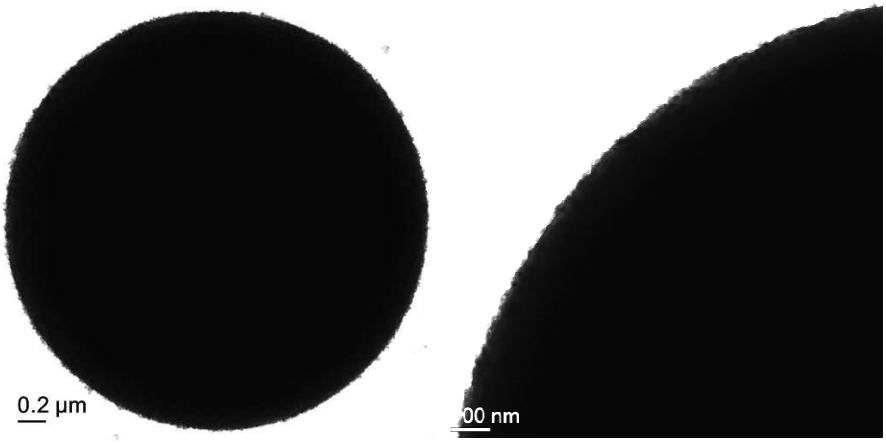

(d)

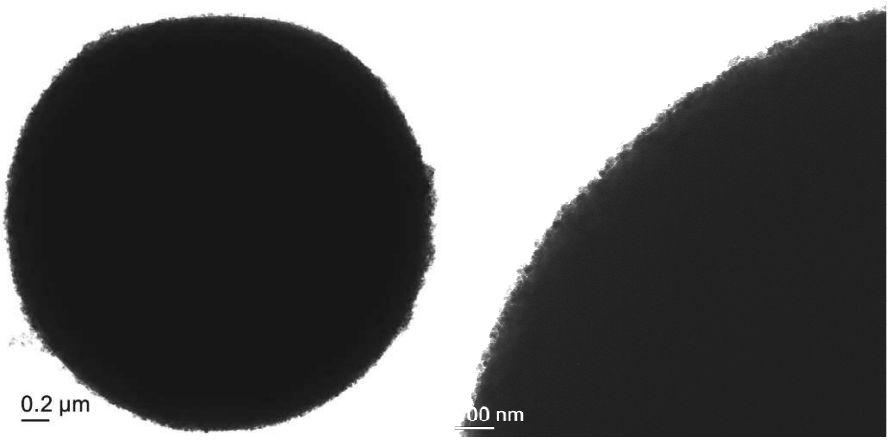

(e)

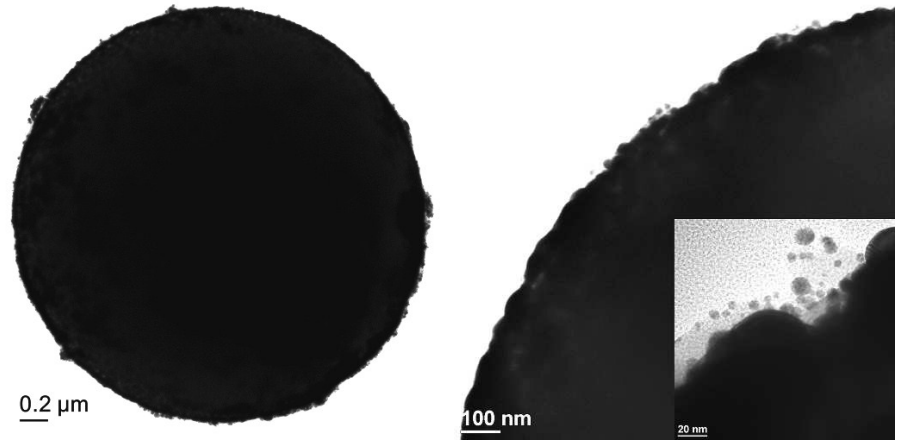

(f)

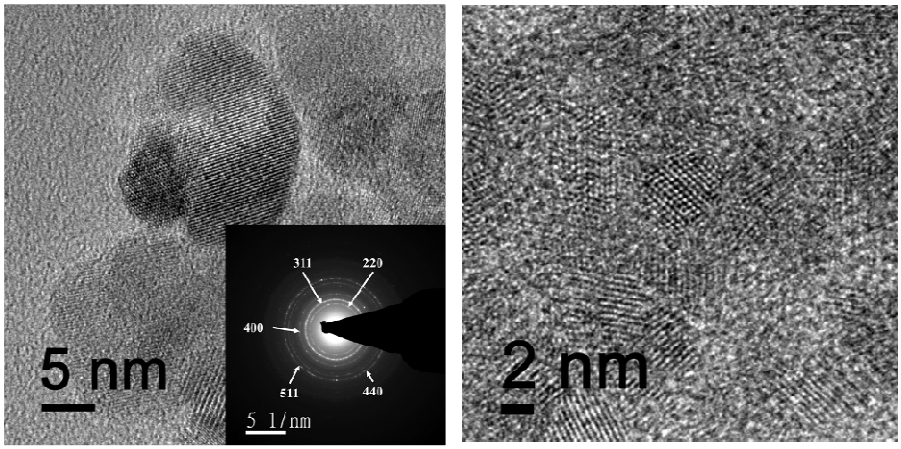

Figure 6

(a)

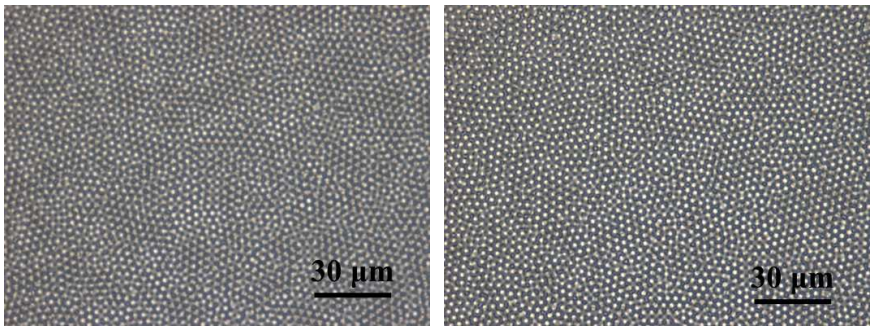

(b)

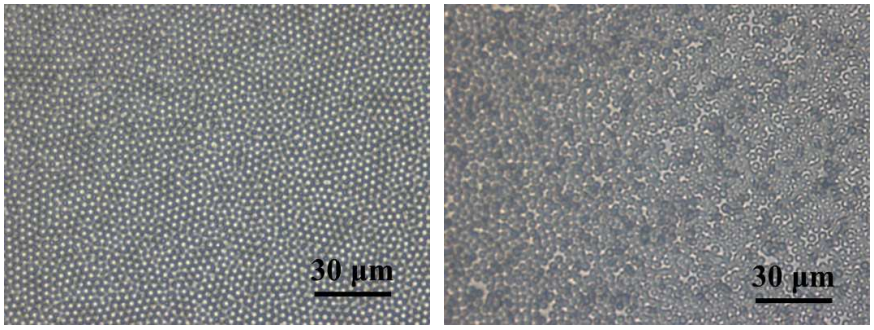

(c)

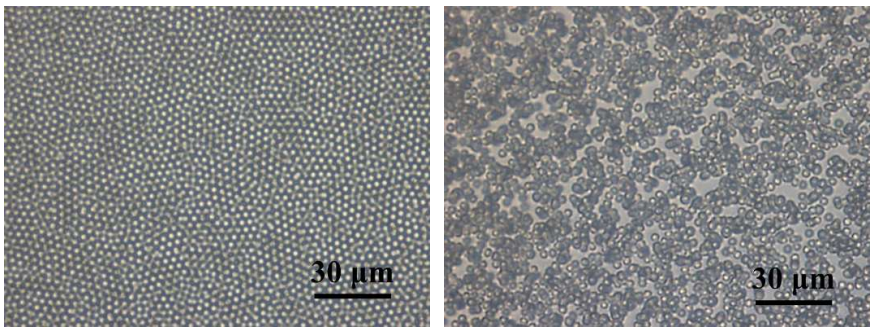

(d)

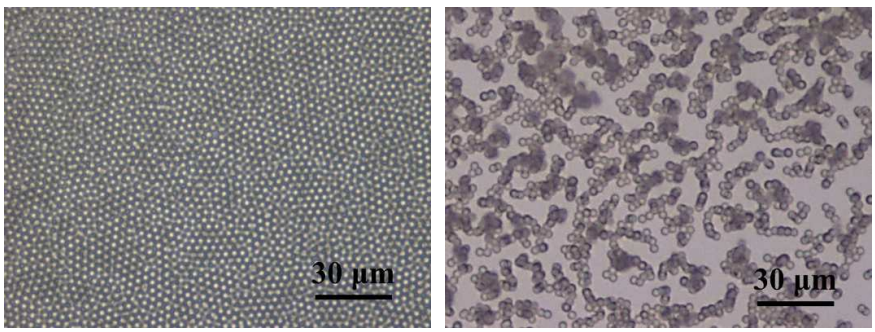

(e)

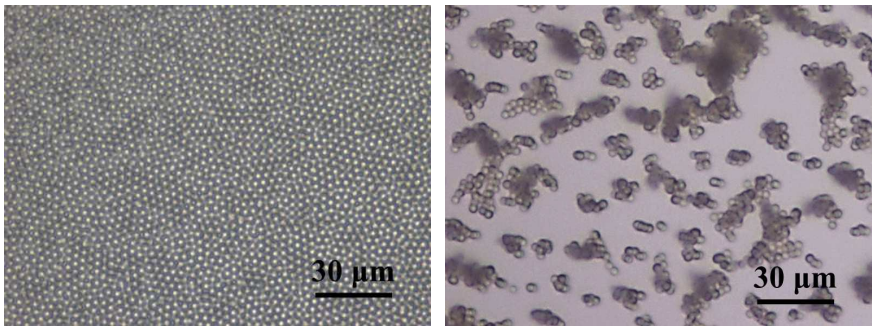

(f)

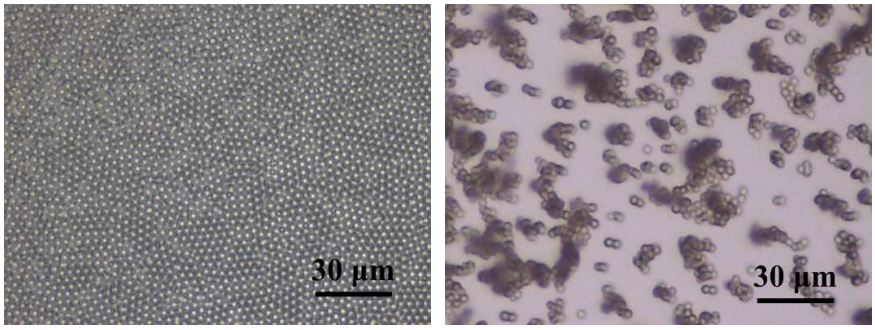

(g)

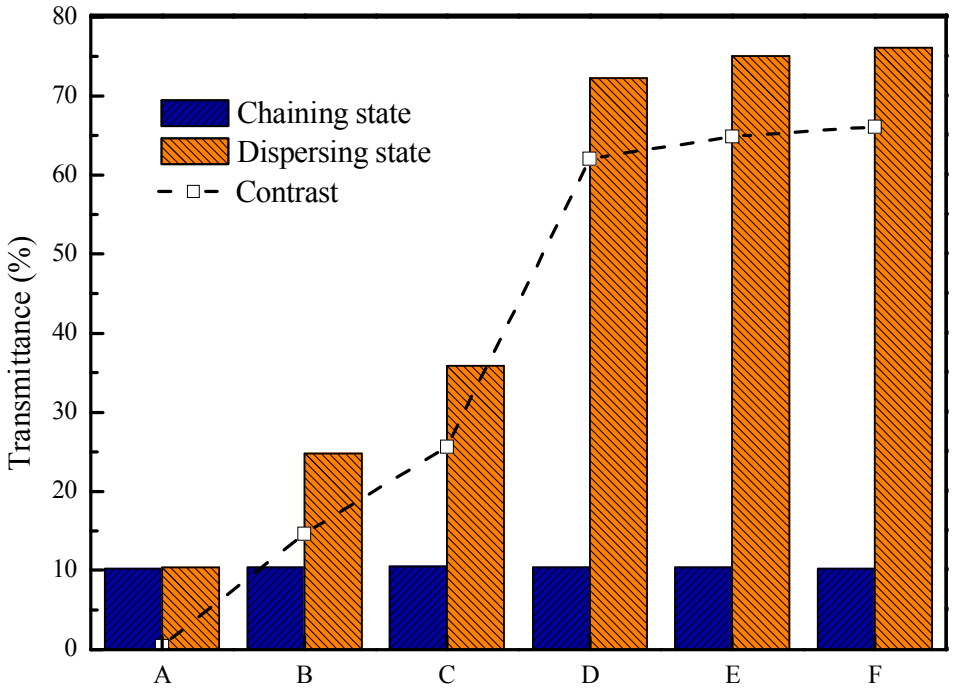

Figure 7

(a)

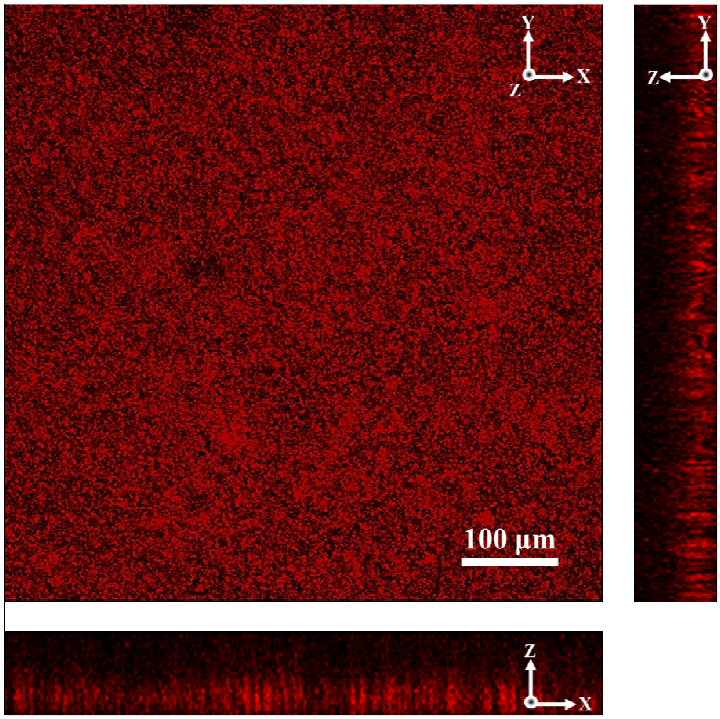

(b)

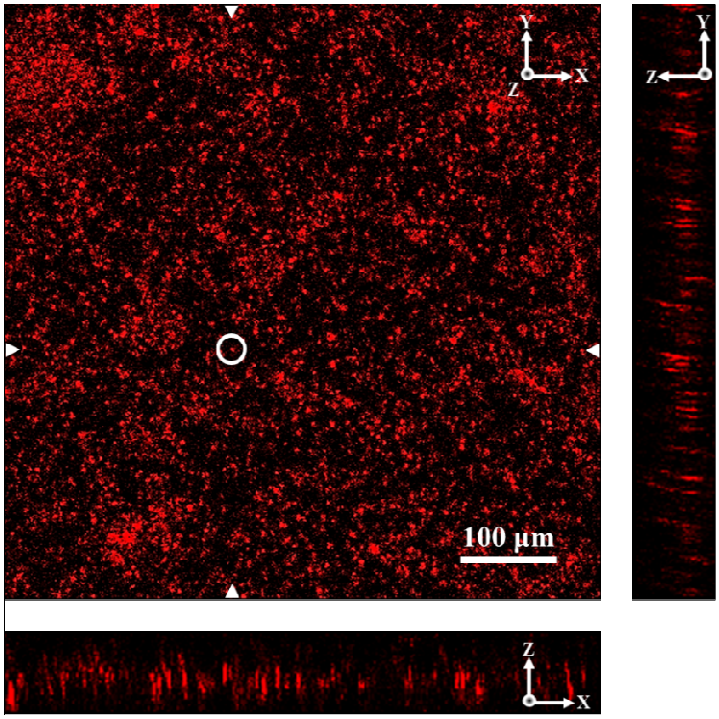

Figure 8

(a)

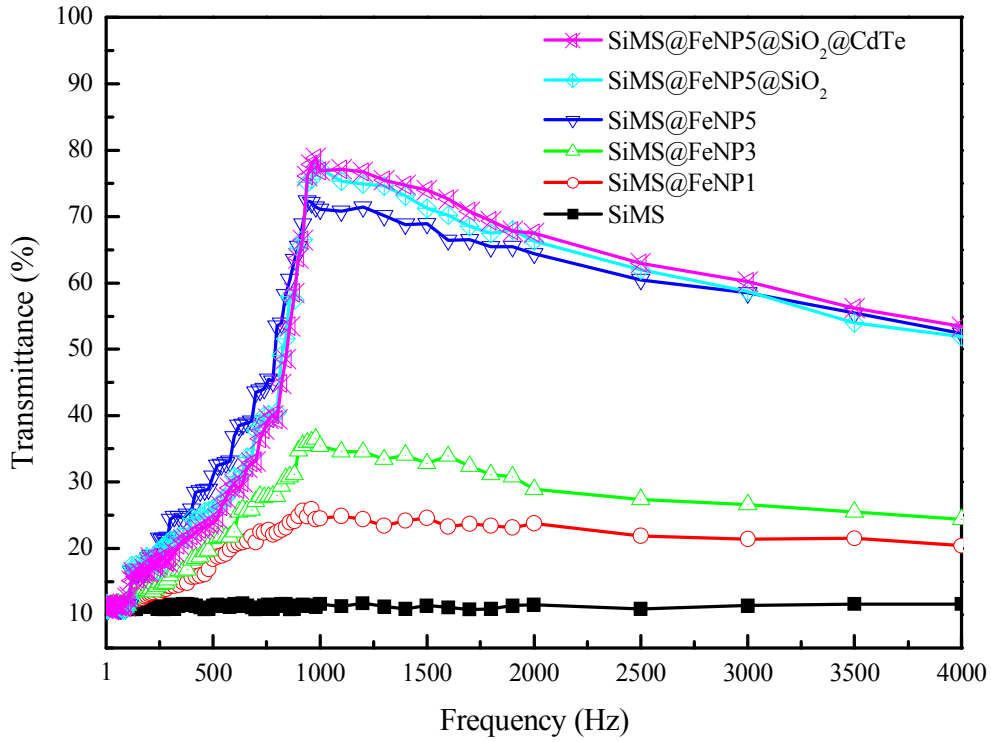

(b)

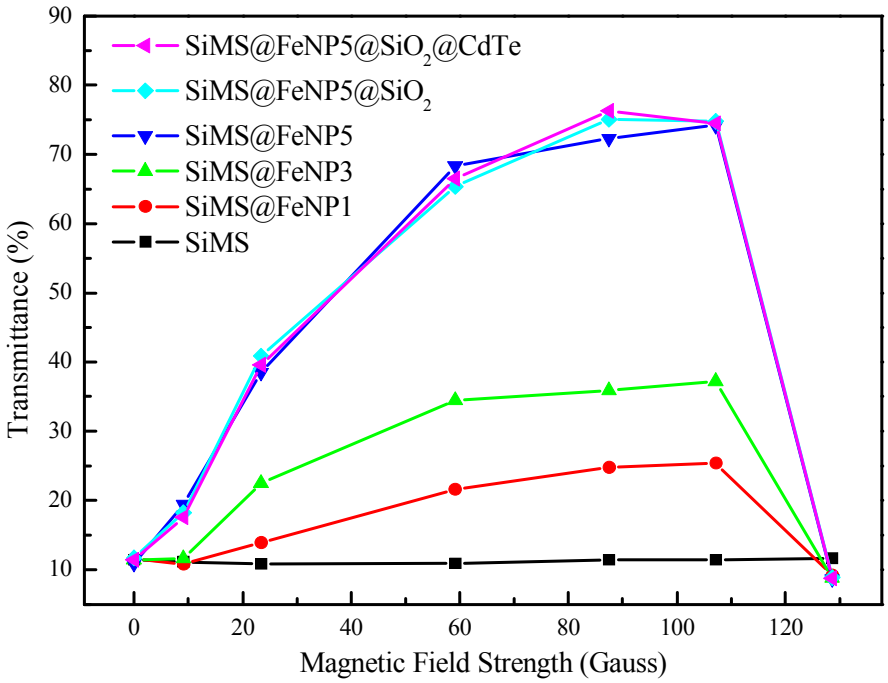

Figure 9

(a)

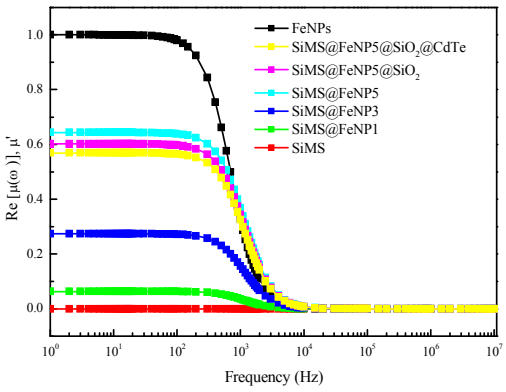

(b)

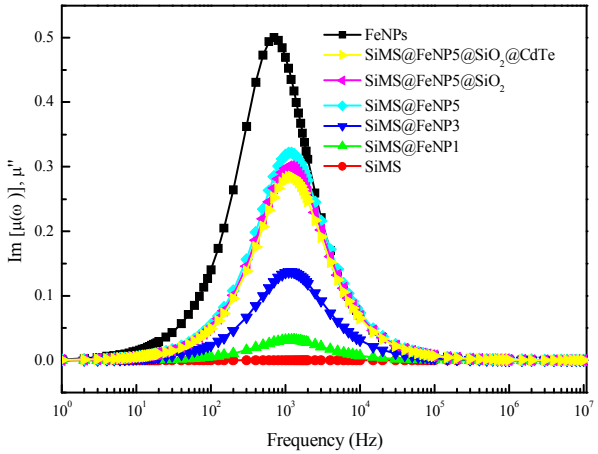

(c)

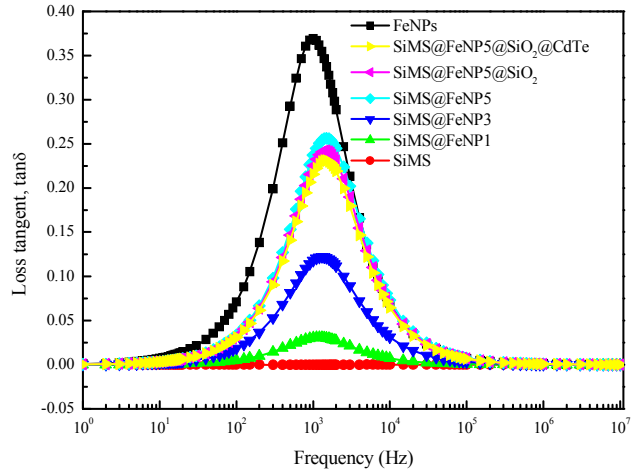

Figure 10

(a)

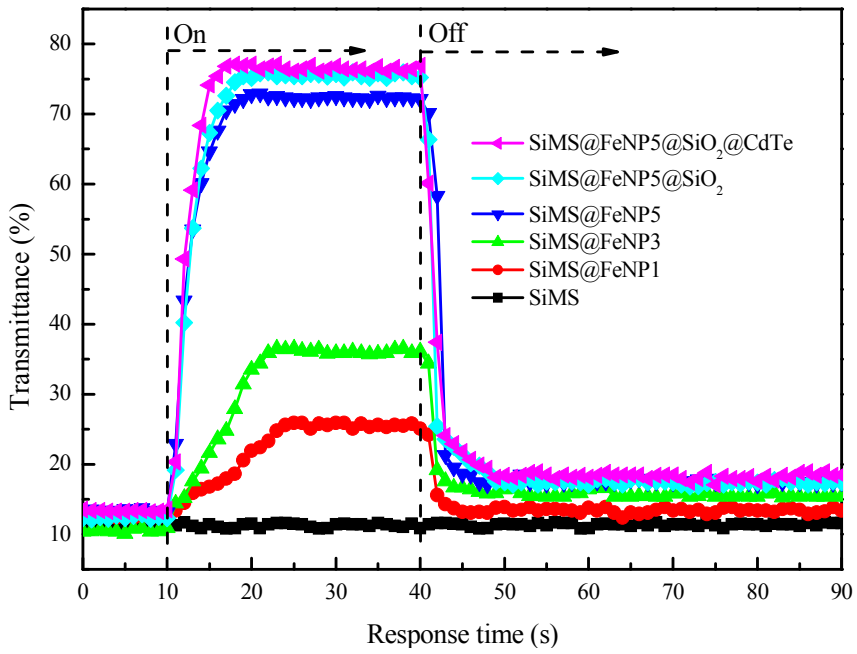

(b)

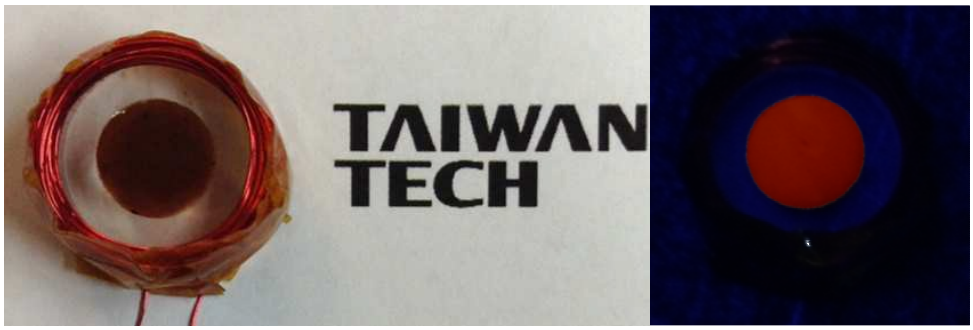

(c)

Table of Contents:

Bifunctional superparamagnetic-luminescent core/shell/satellite structured microspheres are prepared with a layer-by-layer assembly between metal cations and thiol groups for magnetodisplay applications